Received: 8 November 2019 | Revised: 25 January 2020 | Accepted: 27 January 2020

DOI: 10.1002/aoc.5591

Applied Organometallic Chemistry WILEY

FULL PAPER

Synthesis, structural, spectroscopic, and thermal studies of some transition-metal complexes of a ligand containing the amino mercapto triazole moiety

Sanaa M. Emam[1] | **Dina A. Tolan**[1,2] | **Ahmed M. El-Nahas**[1]

[1]Chemistry Department, Faculty of Science, Menoufia University, Shebin el Kom, 32512, Egypt

[2]Department of Chemistry, College of Science and Humanities in Al-Kharj, Prince Sattam bin Abdulaziz University, Al-Kharj, 11942, Saudi Arabia

Correspondence
Dina A. Tolan, Department of Chemistry, College of Science and Humanities in Al-Kharj, Prince Sattam bin Abdulaziz University, Al-Kharj 11942, Saudi Arabia.
Email: d_tolan2005@yahoo.com

A new series of transition-metal complexes of Schiff base ligand containing the amino mercapto triazole moiety (**HL**) was prepared. The Schiff base and its metal complexes were elucidated by different spectroscopic techniques (infrared [IR], ^{1}H nuclear magnetic resonance, UV–Visible, mass, and electron spin resonance [ESR]), and magnetic moment and thermal studies. Quantum chemical calculations have been carried out to study the structure of the ligand and some of its complexes. The IR spectra showed that the ligand is chelated with the metal ion in a neutral, tridentate, and bidentate manner using NOS and NO donors in complexes **1**–**6**, **10**–**12**, and **7** and **8**, respectively, whereas it behaves in a monobasic tridentate fashion using NOS donor sites in copper(II) nitrate complex (**9**). The magnetic moment and electronic spectra data revealed octahedral and square pyramidal geometries for complexes **2**, **11**, **12**, and **5**–**8** and **10**, respectively. However, the other complexes were found to have tetrahedral (**4**), trigonal bipyramidal (**1** and **3**), and square planar (**9**) structures. Thermal studies revealed that the chelates with different crystallized solvents undergo different types of interactions and the decomposition pathway ended with the formation of metal oxygen (MO) and metal sulfur (MS) as final products. The ESR spectrum of copper(II) complex **10** is axial in nature with hyperfine splitting with $^{2}B_{1g}$ as a ground state. By contrast, complexes **7** and **8** undergo distortion around the Cu(II) center, affording rhombic ESR spectra. The **HL** ligand and some of its complexes were screened against two bacterial species. Data showed that complex **12** demonstrated a better antibacterial activity than **HL** ligand and other chelates.

KEYWORDS

1,2,4-triazole, antimicrobial, DFT calculations, metal complexes, Schiff base

1 | INTRODUCTION

The microbial resistance of antibiotics is considered one of the challenges in medicinal chemistry. Designing new antimicrobial agents with different chemical characteristics from those of existing ones is considered a critical demand to overcome this problem. The chemistry of 1,2,4-triazoles and their derivatives have received considerable attention owing to their effective pharmacological activities including antimicrobial, analgesic, antineoplastic, anti-inflammatory, local anesthetic, antineoplastic, anticonvulsant, antineoplastic, antimalarial, antiviral,

antiproliferative, and anticancer properties.[1–3] Further, 1,2,4-triazoles and their derivatives play an important role in agricultural and industrial applications.[4]] Among them, Schiff bases involving the 1,2,4-triazole moiety have attracted wide attention due to their extended biological activities, chemical, physical, and photochromic properties as well as their analytical applications.[5,6] Schiff base metal complexes containing the triazole moiety have been studied because of their use as drugs and their various industrial and biological applications.[7–11]

On the other side, ligands containing pyrazoles have been important compounds because of their surprising structural features, coordination chemistry, momentous physical and chemical properties as well as their pharmacological applications.[12–15]] One of the most important derivatives of antipyrine is 4-aminoantipyrine which shows great applications in medicinal chemistry.[16–18] Schiff bases containing 4-aminoantipyrine and their metal complexes have different biological applications that include antifungal, antibacterial, analgesic, antipyretic, and anti-inflammatory.[16–19] Chelation of organic compounds with metal causes important change in the biological properties of both the metal and the ligand moiety. It has been reported that biological activities of most Schiff bases improved upon coordination with different transition elements, with chelation reported to cure many diseases including cancer.[20–28] In this work, a new Schiff base ligand was prepared by condensation of 4-formyl antipyrine with 3-(3′-pyridyl)-4-amino-5-mercapto-1,2,4-triazole, which was further reacted with Co(II), Ni(II), Cu(II), Zn(II), and Cd(II) metal ions to form the corresponding metal complexes. The Schiff base ligand and its metal complexes were characterized by different analytical and spectroscopic methods. In addition, the antimicrobial activities of some selected compounds were investigated against different types of bacteria. Quantum chemical calculations also have been performed to support and interpret experimental findings.

2 | EXPERIMENTAL

2.1 | Analytical and physical measurements

All chemicals were of analytical grade (BDH or Sigma Aldrich) including all metal salts and were used as obtained without further purification. Elemental analyses (C, H, and N) were performed at the Microanalytical Unit, Cairo University, Egypt. Cobalt(II), nickel(II), and copper(II) ions of metal complexes were estimated by complexometric titration using ethylenediaminetetraacetic acid, whereas cadmium(II) and zinc(II) ions were determined by gravimetric analyses.[29] In addition, the chloride and bromide ions were evaluated by argentometry.[29] Molar conductivity estimations were made in dimethylformamide (DMF) solution (10^{-3} M) using a Tacussel conductometer type CD6N. The ^{1}H nuclear magnetic resonance (NMR) spectra were obtained in dimethyl sulfoxide (DMSO)-d_6 on a Varian XL Gemini 300 spectrophotometer at 300 MHz at room temperature. The infrared spectra were recorded as KBr plates on a Nicolet FT-IR spectrophotometer within the range 4000–400 cm^{-1}. The electronic spectra were obtained as Nujol mulls on a Perkin-Elmer Lambda 4B spectrophotometer. Magnetic susceptibilities were measured at room temperature by the Gouy method using the Johnson Matthey magnetic susceptibility balance. Diamagnetic corrections were determined using Pascal's constants.[30] The effective magnetic moments were ascertained from the relation $\mu_{eff} = 2.84(X_M{}^{corrt}\ T)^{1/2}$, where $X_M{}^{corrt}$ is the molar magnetic susceptibility corrected for diamagnetism of all atoms in the compounds. The thermal analyses (thermogravimetric [TG] and differential thermal analysis [DTA]) were carried out using a Shimadzu DAT/TG-50 thermal analyzer with a heating rate of 10 °C/min under a nitrogen environment with a streaming rate of 20 mL/min from room temperature to 1000 °C utilizing platinum crucibles. The electron spin resonance (ESR) spectra for Cu(II) complexes were obtained using a Varian E-109C model spectrometer outfitted with a field modulation unit at frequency 100 kHz. measurements were affected in the X-band with a microcrystalline powder at room temperature . Melting points were measured using the Stuart melting point apparatus. The antimicrobial activity of **HL** ligand and some of its complexes was estimated against positive bacteria (*Streptococcus pyogenes*) and negative bacteria (*Escherichia coli*).

2.2 | Synthesis of the ligand HL

The **HL** ligand was prepared by a two-step process. The first one involves synthesis of 3-(3′-pyridyl)-4-amino-5-mercapto-1,2,4-triazole and 4-formylantipyrine as reported previously[31,32] (Scheme 1), while the second step is concerned with the preparation of a Schiff base ligand – (E)-1,5-dimethyl-2-phenyl-4-({3-[pyridin-3-yl]-5-thioxo-1,5-dihydro-4H-1,2,4-triazol-4-yl)imino}methyl)-1,2-dihydro-3H-pyrazol-3-one.

The ligand was synthesized by addition of an ethanolic solution (20 mL) containing 4-formylantipyrine (0.40 mmol, 2.16 g) to a hot ethanolic solution (30 mL) containing an equimolar concentration of 3-(3′-pyridyl)-4-amino-5-mercapto-1,2,4-triazole. Then, the reaction

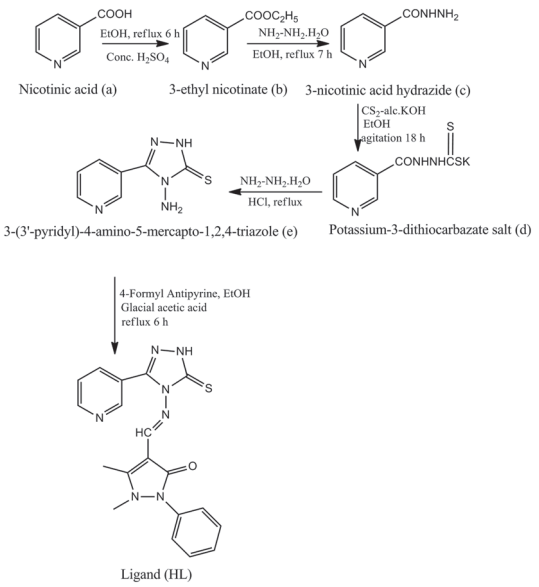

SCHEME 1 Synthesis of 3-(3′-pyridyl)-4-amino-5-mercapto-1,2,4-triazole and 4-formylantipyrine (**HL**)

mixture was refluxed on a water bath for 6 h in the presence of few drops of glacial acetic acid. After that, the reaction mixture was left overnight at room temperature. The resulting off-white solid was filtered off, washed several times with cold ethanol, crystallized from absolute ethanol, and dried under vacuum.

2.3 | Synthesis of HL ligand metal complexes

Ethanolic solution (20 mL) of appropriate metal salt (0.50 mmol) was added dropwise to ethanolic solution (30 mL) containing an equimolar concentration of Schiff base and stirred with gentle warming. The reaction mixture was magnetically stirred under reflux at 60 °C for 6 h and then allowed to cool down at room temperature. Then, the excess of solvent was evaporated under reduced pressure, affording the solid product that was washed with a small volume of ethanol several times and dried over P_2O_5 in vacuum.

2.4 | Antimicrobial activity

The synthesized ligand (**HL**) and some of its metal complexes (**1**, **2**, **4**, **5**, **11**, and **12**) were tested to develop new antimicrobial agents and evaluate their growth inhibitory activity against two reference strains of microscopic organisms (*E. coli* as Gram-negative bacteria and *S. pyogenes* as Gram-positive bacteria) by the disk diffusion method.[33] Amoxicillin was used as the positive standard antibacterial agent and DMSO was employed as the negative control for these bacteria. Bacterial cells were swabbed in 50 mL nutrient broth in a 250-mL flask with vigorous shaking and incubated at 37 °C for 16 h. A sterile glass spreader was used to spread bacterial cultures (100 μL) on nutrient agar plates and cells incubated at 37 °C for 24 h[34,35] The tested compounds were dissolved in DMSO to obtain stock solutions. The required concentrations (100, 200, and 500 mg/mL) were prepared by appropriate dilutions using the stock solutions. The sterile petri dishes containing agar medium were seeded with 0.5 mL of each of the tested bacteria (6×10^3 CFU). After solidification, sterilized filter papers were saturated with 0.1 mL of the tested compounds. Then, the plates were incubated at 37 °C for 24 h, on which clear or inhibition zones were measured (in millimeter). DMSO (0.1 mL) was used as the control for each organism to detect the resulting diameter of inhibition zone.

2.5 | Theoretical methods

The quantum mechanical study using the density functional theory (DFT)[36,37] was carried out using the Gaussian 98W[38] package. Geometrical optimizations were carried out at the B3LYP functional[39–41] level with the 3-21G(d) basis set. All the calculations were performed in the gas phase. Frequency calculations were performed for all optimized geometries at the same level of theory to verify their nature as minima or transition states on the potential energy surface of these systems. The absence of negative eigenvalues in the force constant matrices indicates that all of the obtained stationary points are minimal. The distribution of the highest occupied and lowest unoccupied frontier molecular orbitals (FMOs; i.e. highest occupied molecular orbital [HOMO] and lowest unoccupied molecular orbital [LUMO], respectively) and the molecular electrostatic potential (MEP) of the ligand and complexes were analyzed. The Chemcraft program[42] was used for displaying the computational results and plotting FMOs.

3 | RESULTS AND DISCUSSION

3.1 | Chemistry

The preparation of 3-(3′-pyridyl)-4-amino-5-mercapto-1,2,4-triazole involved four steps as illustrated in Scheme 1. Initially, nicotinic acid (a) was esterified using ethyl alcohol to obtain 3-ethyl nicotinate (b) which is converted to 3-nicotinic acid hydrazide (c) using hydrazine hydrate.

The formed hydrazide was then reacted with carbon disulfide in the presence of alcoholic KOH to form potassium-3-dithiocarbazate salt (d), followed by the addition of hydrazine hydrate and HCl to obtain 3-(3′-pyridyl)-4-amino-5-mercapto-1,2,4-triazole. The novel Schiff base was prepared by refluxing an ethanolic solution containing an equimolar concentration of 3-(3′-pyridyl)-4-amino-5-mercapto-1,2,4-triazole and 4-formyl antipyrine. The structure of the ligand was elucidated using elemental analyses and spectral methods. Moreover, the ligand was utilized for chelation with various metal(II) salts having different geometrical structures. All the solid metal chelates were steady at room temperature; nonhygroscopic; partially soluble in most organic solvents, such as chloroform, methanol, ethanol, and acetonitrile; and completely soluble in DMSO and DMF. The molar conductance value of the metal complexes in DMF solution (10^{-3} M), except that of complexes **2**, **4**, and **7–9** (Table 1), of 12–42 Ω^{-1} cm^2 mol^{-1} revealed that all complexes are nonelectrolytes, and their ions are directly coordinated to metal ions,[43,44] whereas the value of 59–83.8 Ω^{-1} cm^2 mol^{-1} for complexes **2**, **4**, and **7–9** typified the 1:1 electrolyte composition.[43]

3.2 | Infrared studies

The IR spectral results of **HL** ligand, its metal complexes, and their assignments are summarized in Table 2. An investigation of the **HL** ligand spectrum (Figure S1) revealed several fundamental weak-broad bands at 3434, 3120 and 3229, 3018 and 3061, 2917 and 2820, and 2760 and 2566 cm^{-1}, which are assigned to stretching vibrations of the adsorbed water molecule, υ(N–H), aromatic and aliphatic C–H, and stretching vibration of the SH group,[45–47] respectively. Furthermore, the spectrum shows a band at 1291 cm^{-1} assignable to ν_{as}(C=S). The additional bands located at 1433 and 1390, 1025 and 1073, and 698 and 757 cm^{-1} are restricted to bending deformation of CH_3 groups, (C–H) in-plane deformation, and out-of-plane (C–H) bending for the aromatic benzene skeleton, respectively.[48,49] Moreover, the **HL** spectrum displays strong and medium bands at 1602, 961, 627 and 426, and 1542 and 1498 cm^{-1} assignable to aromatic ν(C=C), pyridine ring breathing, C–H in-plane and out-of-plane pyridine ring bending along with triazole ring stretching, and NH in-plane deformation vibration, respectively.[50,51] In addition, the IR spectrum of **HL** ligand illustrates strong and medium bands at 1661 and 1125, 583 cm^{-1} attributed to the C=O stretching and in-plane, out-of-plane bending vibrations (υ and δ, γ) of the antipyrine carbonyl group, respectively.[20] For the free ligand, four bands appeared at 1542, 1333, 1073, and 827 cm^{-1} attributable to thioamide I {δ (NH) + ν(C=N)}, thioamide II {ν(C=N) + ν_{as}(C=S)}, thioamide III{ν(C–N)- + ν_s(C=S)}, and thioamide IV that is mainly from δ(C=S).[52,53] Moreover, the ligand spectrum displays a high-intensity band at 1585 cm^{-1} assignable to the stretching frequency of the azomethine group ν(C=N).[54] Therefore, the ligand contains NCSH and NHCS groups with the expectation of delocalized thioamide vibrations. In addition, the appearance of weak bands characteristic of NH, SH, and C=S groups suggested that Schiff base exhibits thiol–thione tautomerism.

The spectra of all metal complexes except complex (**9**) revealed the absence of ν(S–H) (2566 cm^{-1}) and the existence of ν(N–H) bands in the region 3110–3292 cm^{-1}, indicating their existence in the thione form (Figures S2–S12). The disappearance of ν(S–H) and ν(N–H) bands in complex **9** (Table 2) confirms the loss of a proton by thioenolization of the SH group. This is further confirmed by the existence of new bands at 747 and 1513 cm^{-1} due to ν(C–S) and ν(C=N), respectively.[27,55] For all complexes except **7** and **8**, the thioamide bands I, II, and III show change in their intensity and position compared with those of the ligand, whereas the thioamide IV band, which mainly arises from δ(C=S), undergoes downshift by 4–18 cm^{-1} in all complexes except **7** and **8** (Table 2), suggesting the coordination of the metal ion with the sulfur atom of the C=S group. The δ(C=S) band does not have a change in its shape and position upon chelation in complexes **7** and **8**. Further, the ν(C=S) stretching frequency of the ligand (1291 cm^{-1}) undergoes upshift at 5–29 cm^{-1} in all complexes except **7–9**, supporting its participation in complex formation. For complex **9**, the spectrum does not show any characteristic bands for the thioamide group (I, II, III, and IV), indicating that the **HL** ligand coordinates with the Cu(II) ion with the deprotonated SH group. The antipyrine carbonyl vibrations (ν and δ) are shifted to lower and higher frequencies at 20–28 and 8–25 cm^{-1}, respectively, implying that the metal binds with the oxygen atom of the carbonyl group. The bands due to ν_{as} and ν_s of the acetate group are displayed within the ranges 1590–1598 and 1404–1420 cm^{-1}, respectively, in complexes **3**, **6**, and **10**. The difference between the two bands (173–186 cm^{-1}) can be taken as an evidence for the monodentate character.[56–59] In complexes **2**, **5**, **9**, and **12**, the ν_{as} (NO_3^-) was observed at 1447, 1448, 1450, and 1444 cm^{-1}, whereas the ν_s (NO_3^-) appeared at 1266, 1273, 1270, and 1260 cm^{-1}, respectively; their separation is small in accordance with the monodentate character of the nitrate group.[54] By contrast, the spectra of complexes **2** and **9** exhibited bands at 1380 cm^{-1}, which can be attributed to the ionic nitrate.[60] The nonligand bands occurring in the 561–606 and 446–525 cm^{-1} ranges have

TABLE 1 Elemental analysis, color, and molar conductance of the **HL** ligand and its metal complexes

No.	Compound	Color	Empirical formula/weight	MP (°C)	Λ_M[a]	Elemental analysis found (Calcd.) %				
						C	H	N	M	X
	$H_2L{\cdot}H_2O$	Off white	$C_{19}H_{19}N_7O_2S$/409.41	230	–	55.56 (55.70)	4.75 (4.68)	24.19 (23.95)	–	–
1	$[Co(HL)Cl(OH)]{\cdot}3.5H_2O$	Blue	$C_{19}H_{25}N_7O_{5.5}SCoCl$/565.89	211	35.5	39.47 (40.33)	4.29 (4.45)	18.25 (17.33)	10.31 (10.41)	5.90 (6.27)
2	$[Co(HL)(OH)(H_2O)_2]NO_3{\cdot}1.75H_2O$	Pink	$C_{19}H_{25.5}N_8O_{8.75}SCo$/596.90	234	83.8	38.10 (38.23)	4.28 (4.31)	19.52 (18.77)	8.92 (9.88)	–
3	$[Co(HL)(OAc)(OH)]{\cdot}4.25H_2O{\cdot}0.25EtOH$	Brown	$C_{21.5}H_{31}N_7O_{8.5}SCo$/614.46	>360	24.0	41.93 (42.03)	4.89 (5.09)	16.50 (15.96)	9.58 (9.59)	–
4	$[Ni(HL)Cl]Cl{\cdot}4.5H_2O$	Green	$C_{19}H_{26}N_7O_{5.5}SNiCl_2$/602.17	>360	69.0	37.70 (37.89)	3.95 (4.35)	17.09 (16.28)	9.87 (9.74)	11.59 (11.79)
5	$[Ni(HL)(NO_3)_2]{\cdot}4.5H_2O$	Green	$C_{19}H_{26}N_9O_{11.5}SNi$/655.18	>360	41.2	34.61 (34.83)	3.19 (4.00)	20.22 (19.24)	8.79 (8.96)	–
6	$[Ni(HL)(OAc)(OH)]{\cdot}4H_2O{\cdot}0.25EtOH$	Olive green	$C_{21.5}H_{30.5}N_7O_{8.25}SNi$/609.73	>360	14.0	42.12 (42.35)	4.51 (5.04)	16.82 (16.08)	9.46 (9.63)	–
7	$[Cu(HL)(OH)(H_2O)_2]Cl{\cdot}4H_2O$	Green	$C_{19}H_{30}N_7O_8SCuCl$/615.50	205	69.0	37.04 (37.08)	4.41 (4.91)	15.91 (15.93)	10.80 (10.32)	5.65 (5.77)
8	$[Cu(HL)(OH)(H_2O)_2]Br{\cdot}3.5H_2O{\cdot}0.25EtOH$	Greenish brown	$C_{19.5}H_{30.5}N_7O_{7.75}SCuBr$/662.51	259	77[b]	35.37 (35.35)	4.20 (4.64)	14.90 (14.80)	9.69 (9.58)	11.99 (12.08)
9	$[Cu(L)(H_2O)]NO_3{\cdot}4.25H_2O$	Greenish brown	$C_{19}H_{26.5}N_8O_{9.25}SCu$/610.48	219	59.0	37.29 (37.38)	4.05 (4.38)	19.80 (18.36)	10.61 (10.41)	–
10	$[Cu(HL)(OAc)(OH)]{\cdot}2.25H_2O$	Greenish brown	$C_{21}H_{25.5}N_7O_{6.25}SCu$/571.48	238	30.0	44.7 (44.14)	4.30 (4.50)	17.63 (17.16)	11.41 (11.11)	–
11	$[Zn(HL)Cl(OH)(H_2O)]{\cdot}6.5H_2O$	Yellowish white	$C_{19}H_{33}N_7O_{9.5}SZnCl$/644.40	233	23.6	35.08 (35.41)	4.99 (5.16)	15.81 (15.22)	10.07 (10.15)	5.19 (5.51)
12	$[Cd(HL)(NO_3)_2(H_2O)]{\cdot}2.25H_2O{\cdot}0.25EtOH$	Yellowish white	$C_{19.5}H_{25}N_9O_{10.5}SCd$/697.88	195	12.0	33.72 (33.56)	3.09 (3.61)	18.93 (18.06)	15.98 (16.11)	–

[a]Unit of Λ_M is ($S{\cdot}cm^2\ mol^{-1}$).
[b]Λ_M in dimethylformamide.

TABLE 2 Infrared spectral bands (cm^{-1}) of the **HL** ligand and its metal complexes

No.	Compound	νOH	νNH (δNH + triazole ring)	νSH	ν(C=O) δ(C=O)	ν(C=N)$_{az}$ Triazole + I	Thioamide group II + ν(C=S)	Thioamide group III + ν(N–N)	Thioamide group IV	Py. ring breathing, C–H in-plane, and out plane bending	Other bands	ν(M–N) ν(M–O) γ(C=O)
	$H_2L{\cdot}H_2O$	3434br	3229w	2566	1661s	1585s	1333m	1073m	827m	961w	–	–
			3120w		1125m	1542s	1291s			627m		–
			1498m							426m		583w
1	$[Co(HL)Cl(OH)]{\cdot}3.5H_2O$	3417br	3200w	–	1633s	1591w	1337w	1053m	809w	976w	–	457w
			3100w		1150w	1549s	1296w			635 m		512w
			1496m									602w
2	$[Co(HL)(OH)(H_2O)_2]NO_3{\cdot}1.75H_2O$	3530sh	3148w	–	1638s	1595m	1317w	1082w	825m	986w	1447[b]	493w
		3450br	1499m		1144m	1549m	1303m	1053w		624w	1380s	520w
											1266 m	602w
3	$[Co(HL)(OAc)(OH)]{\cdot}4.25H_2O{\cdot}0.25EtOH$	3366br	3188w	–	1634s	1579m	1342w	1088w	798m	960sh	1592	446w
			1493w		1132w	1535m	1293w	1053w		623w	1409[a]	509w
												603w
4	$[Ni(HL)Cl]Cl{\cdot}4.5H_2O$	3386br	3183w	–	1641s	1594w	1317w	1079w	821w	984w	–	448w
			1498m		1142m	1546m	1290m	1048w	800sh	621w		505w
					1111w							603w
5	$[Ni(HL)(NO_3)_2]{\cdot}4.5H_2O$	3425br	3152w	–	1641s	1595m	1320w	1082w	825m	987w	1448[b]	499w
			1500m		1145m	1549m	1304w	1052w		625m	1273w	525w
					1100sh							604w
6	$[Ni(HL)(OAc)(OH)]{\cdot}4H_2O{\cdot}0.25EtOH$	3351br	3170w	–	1648s	1568m	1345w	1068w	818w	950sh	1590[a]	455w
			1494w		1136w	1538m	1290w		770w	622w	1404	510w
												594w
7	$[Cu(HL)(OH)(H_2O)_2]Cl{\cdot}4H_2O$	3421br	3270br	–	1636s	1591w	1317w	1079w	826m	980w	–	459w
			1491m		1133w	1542m	1290w	1052w		628w		509w
												606w
8	$[Cu(HL)(OH)(H_2O)_2]Br{\cdot}3.5H_2O{\cdot}0.25EtOH$	3419br	3292br		1635s	1595w	1317w	1070w	827m	984w	–	456w
			1487m		1147w	1542m	1290w	1051w		631m		504w
												605w

(Continues)

TABLE 2 (Continued)

No.	Compound	νOH	νNH (δNH + triazole ring)	νSH	ν(C=O) δ(C=O)	ν(C=N)$_{az}$ Triazole + I	Thioamide group II + ν(C=S)	III + ν(N–N)	IV	Py. ring breathing, C–H in-plane, and out plane bending	Other bands	ν(M–N) ν(M–O) γ(C=O)
9	$[Cu(L)(H_2O)]NO_3{\cdot}4.25H_2O$	3419br	–	–	1636s	1595w	–	–	–	987m	1450[b]	457w
					1146m	1548s		1052m		629m	1379	503w
			1499w								1270w	605w
10	$[Cu(HL)(OAc)(OH)]{\cdot}2.25H_2O$	3405br	3289w	–	1634s	1572m	1300w	1055w	812m	964w	1598[a]	465w
			3158w		1146w	1550sh	1315s	1043w	786w	630m	1420	510w
			1490 m									597 m
11	$[Zn(HL)Cl(OH)(H_2O)]{\cdot}6.5H_2O$	3443br	3202w	–	1635s	1587w	1344w	1053m	844m	975w	–	456w
			1498m		1151w	1552s	1320w		821w	635w		511w
												605w
12	$[Cd(HL)(NO_3)_2(H_2O)]{\cdot}2.25H_2O{\cdot}0.25$ EtOH	3423br	3110w	–	1639s	1595m	1343m	1081w	823m	981m	1444m[b]	488w
			1500w		1142m	1546m	1313m	1054m		626w	1260 m	511w
												600w

[a]Acetate ion: ν_{as} (CH_3COO^-), ν_s (CH_3COO^-); nitrate ion: ν_{as} (NO_3^-), ν_s (NO_3^-).

been assigned to ν(M–O) and ν(M–N), respectively.[46,48,61] The existence of coordination and/or lattice water molecules in the chelates is indicated by a broad band within the range 3351–3530 cm^{-1}, which can be attributed to ν(OH) of the water molecules[44] and confirmed using thermal analyses.

These arguments show that the ligand exhibits thione–thiol tautomerism as given in Figure 1. The existence of thioamide bands in the IR spectra of the free ligand and its complexes except **9** indicates that they exist as thione tautomer in the solid state, which is in agreement with previous studies on the triazole family.[52,53,55] The IR data established that the ligand reacts with the metal ions in a neutral tridentate manner through NOS sites in all complexes except **7–9**. By contrast, the ligand binds with Cu(II) ion in a neutral bidentate manner via NO donors and behaves as monobasic tridentate via NOS in complexes **7–9**, respectively.

3.3 | ^{1}H NMR spectra of HL ligand and its cadmium complex

The ^{1}H NMR spectral data of **HL** ligand reveals two singlet signals in the range of δ 2.49–2.56 and 3.31–3.37 ppm assigned to three protons of C–CH_3 and N–CH_3, respectively.[20] The NH and the azomethine proton signals were observed at δ 9.33 and 9.17 ppm in the spectrum of the ligand.[31,62]] Besides, two doublets and one singlet along with multiplet signals appeared in the range of δ = 8.70–8.72, 7.58–7.60, and 8.28–8.31 ppm, and these are attributed to four pyridine protons.[63] By contrast, the signals corresponding to the five aromatic protons are observed within range δ = 7.38–7.54 ppm.[64] In the spectrum of Cd(II) complex, the peak corresponding to –SH (11.12 ppm) is not observed, but another signal appeared at δ 9.98 ppm, which was assignable to the NH group. This clearly indicates the thione form for the ligand during complex formation, confirming the participation of sulfur atom of the C=S group in chelation. The signal due to the azomethine proton undergoes upfield shift, pointing to the coordination of the azomethine nitrogen with Cd(II) ion. In addition, the aromatic proton signals are found at δ = 7.38–8.88 ppm, showing slight shift upon chelation.

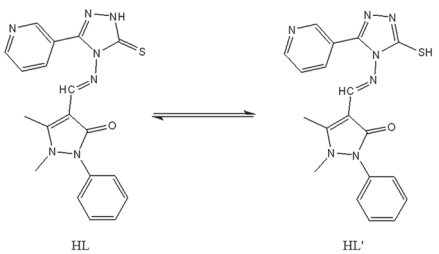

FIGURE 1 Structure of ligand (**HL**) and its thiol form (**HL′**)

3.4 | Mass spectra of complexes

Fast atom bombardment (FAB) mass spectroscopy analysis of complexes $CoCl_2$, $Co(NO_3)_2$, and $Ni(OAc)_2$ (Figures S13–S15) were performed. The molecular ion peaks observed for these complexes were found to be at m/e = 565.89, 596.90, and 590.30, respectively, indicating that they have a monomeric nature. The spectrum of the cobalt(II) chloride complex (Scheme 2) displayed species at m/e = 564, 560, 485.1, 392.1, 214.2, and 179.2 amu, pointing to $[C_{19}H_{25}N_7O_{5.5}SCoCl]^+$, $[C_{19}H_{24.5}N_7O_{5.25}SCoCl]^+$, $[C_{19}H_{20}N_7O_3SCo]^+$, $[C_{19}H_{17}N_7OS]^+$, $[C_9H_7N_5S]^+$, and $[C_7H_6N_4S]^+$, respectively. The spectrum of cobalt(II) nitrate complex showed fragments at m/e = 563, 512, 466.2, 392.1, 266.2, 214.2, and 179.2 amu, referring to $[C_{19}H_{22}N_8O_7SCo]^+$, $[C_{19}H_{21}N_7O_{4.5}SCo]^+$, $[C_{19}H_{18}N_7O_2SCo]^+$, $[C_{19}H_{17}N_7OS]^+$, $[C_{17}H_6N_5OS]^+$, $[C_9H_6N_5S]^+$, and $[C_7H_6N_4S]^+$, respectively. Furthermore, the FAB spectrum of nickel(II) acetate chelate denotes different fragmentations (Scheme 3) at m/e = 590.3, 562.0, 488.8, 451.0, 392.1, 308.8, 214.2, and 179.2 amu, corresponding to $[C_{21}H_{28}N_7O_{7.5}SNi]^+$, $[C_{21}H_{25}N_7O_6SNi]^+$, $[C_{19}H_{20.5}N_7O_{3.25}SNi]^+$, $[C_{19}H_{17}N_7OSNi]^+$, $[C_{19}H_{17}N_7OS]^+$, $[C_{13}H_7N_7OS]^+$, $[C_8H_5N_6S]^+$, and $[C_7H_6N_4S]^+$, respectively. Inside the spectra of all complexes, the fundamental peak, which has the higher intensity and appears at 392.1 amu, represents the more steady, charged fragment ion in Schiff base (**HL**).

3.5 | Electronic absorption spectra

The ultraviolet and visible spectral data in Nujol mull and magnetic moments of metal complexes are collected and presented in Table 3. The ultraviolet spectra of all complexes usually show two absorption maxima at 239–255 nm and 287–326 and 345–432 nm. The absorption at 287–326 nm is due to the presence of the chromophore group (C=S).

3.5.1 | Cobalt complexes

Cobalt(II) complexes **1**, **3**, and **2** showed magnetic moment values 4.82, 4.9, and 5.1 BM at room temperature, suggesting high-spin trigonal bipyramidal (TBP) and octahedral structures.[64] The electronic spectra of complexes **1** and **3**, $[Co(HL)Cl(OH)]\cdot 3.5H_2O$, and

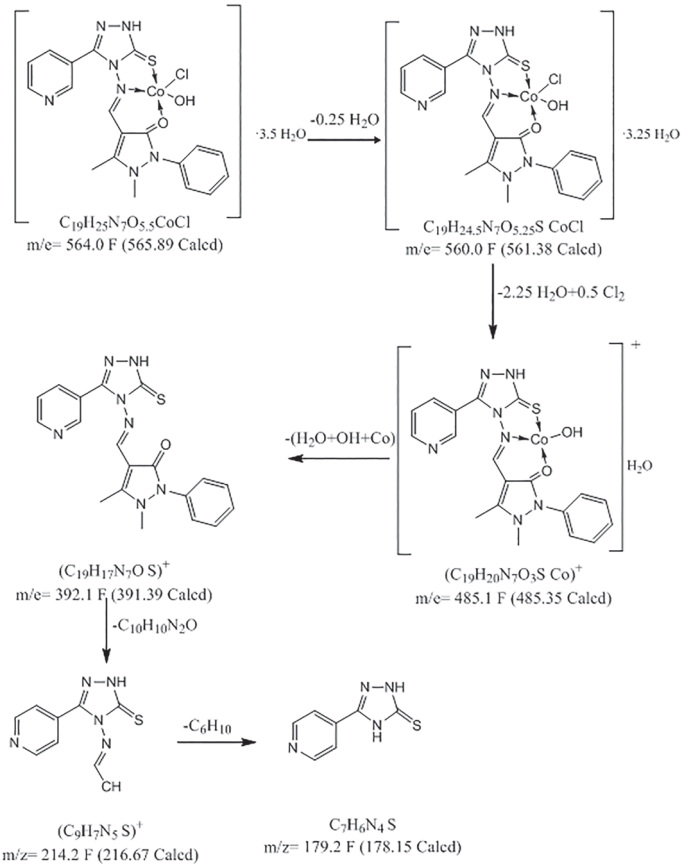

SCHEME 2 Proposed mass fragmentation of complex **1**

$[Co(HL)(OAc)(OH)]\cdot 4.25H_2O\cdot 0.25EtOH$ depict bands at 695–751, 542–632, and 498–502 nm assignable to $^4A'_2(F) \rightarrow {}^4E'$ (F), $^4A'_2(F) \rightarrow {}^4E''(P)$, and $^4A'_2(F) \rightarrow {}^4A_2'(P)$ transitions, respectively. These transitions are indicative of high-spin TBP geometry around the cobalt(II) ion.[64] By contrast, the electronic spectrum of complex **2** $[Co(HL)(OH)(H_2O)_2]NO_3\cdot 1.75H_2O$ displays absorption bands at 801, 524, and 502 nm assignable to $^4T_{1g}(F) \rightarrow {}^4T_{2g}(F)$ (υ_1), $^4T_{1g}(F) \rightarrow {}^4A_{2g}(F)$ (υ_2), and $^4T_{1g}(F) \rightarrow {}^4T_{1g}(P)$ (υ_3) transitions, indicating to high-spin octahedral geometry around the cobalt(II) ion.[65]

3.5.2 | Nickel complexes

The room temperature magnetic moment values of nickel(II) complexes **4**, **5**, and **6** were estimated at 3.23, 3.36, and 3.52 BM, respectively. These values were within the range except for tetrahedral and square pyramidal (SP) geometries for mononuclear Ni(II) complexes.[64] The electronic spectra of isostructural nickel(II) complexes **5** and **6** displayed three broad peaks that appeared within ranges 789–805, 622–664, and 432–435 nm assignable to $^2B_{1g} \rightarrow {}^2A_{1g}$, $^2B_{1g} \rightarrow {}^2B_{2g}$, and $^2B_{1g} \rightarrow {}^2E_g$ transitions, respectively. This indicated an SP structure around the nickel(II) ion.[64] Meanwhile, the spectrum of complex **4** revealed three electronic absorption peaks at 857, 795, and 658 nm attributable to $^3T_1(F) \rightarrow {}^3T_2(F)$, $^3T_1(F) \rightarrow {}^3T_1(P)$, and $^3T_1(F) \rightarrow {}^3A_2(F)$ nm transitions, respectively. This is consistent with the tetrahedral geometry around the nickel(II) ion.[48,66]

3.5.3 | Copper complexes

Complexes **7**, **8**, and **10** depict three absorption bands at 800–811, 690–769, and 440–550 nm, which were attributed to $^2B_{1g} \rightarrow {}^2A_{1g}$, $^2B_{1g} \rightarrow {}^2B_{2g}$, and $^2B_{1g} \rightarrow {}^2E_g$ transitions, respectively, affording distorted SP geometry around the Cu(II) ion.[67] However, complex **9** displays two bands at 665 and 502 nm assignable to $^2B_{1g} \rightarrow {}^2B_{2g}$ and $^2B_{1g} \rightarrow {}^2E_g$ transitions, respectively, pointing to the distorted square planar structure around the copper(II) ion.[46,67,68] The magnetic moment values for copper(II) complexes **7–10** fall in the range 1.75–2.1 BM.

Based on elemental analyses and spectral methods, the suggested chemical structures for the synthesized metal complexes are represented in Figure 2.

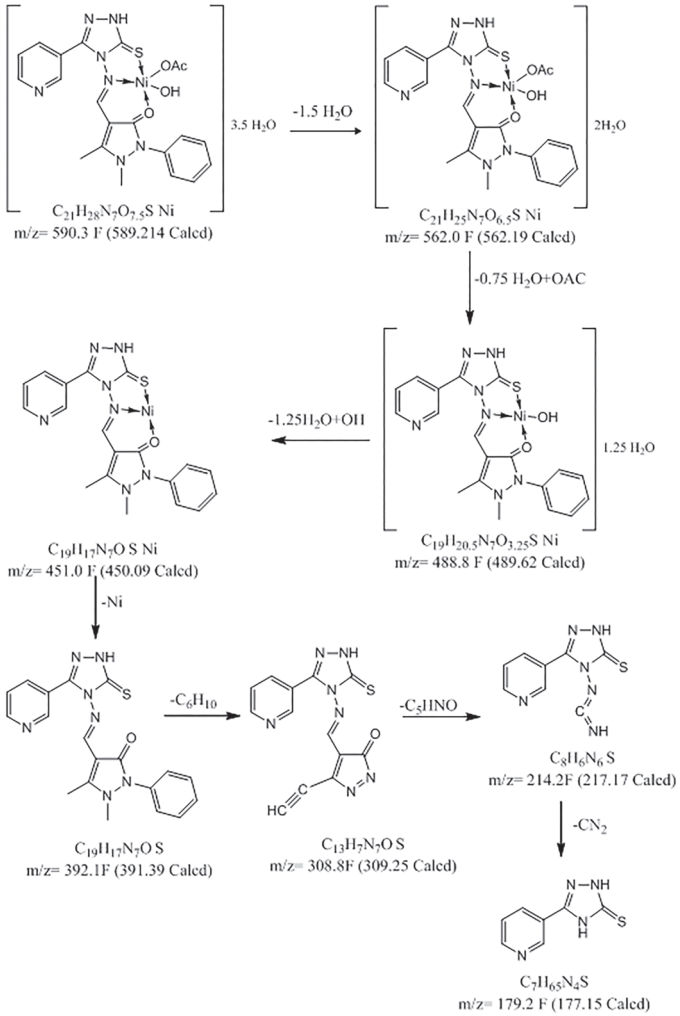

SCHEME 3 Proposed mass fragmentation of complex **6**

3.5.4 | Ligand field parameters

The ligand field parameters for high-spin octahedral cobalt(II) complex **2**, including ligand field splitting energy ($10D_q$), Racah interelectronic repulsion (B), nephelauxetic ratio [$\beta = B/B_o$, where B_o for free Co(II) ion is 971 cm^{-1}], and ligand field stabilization energy (LFSE), were calculated using ν_3/ν_1 and ν_3/ν_2 ratios.[66] The results demonstrated that the inter-electronic repulsion factor of complex **2** is 688 cm^{-1}, which is smaller than that of the free ion, indicating a considerable orbital overlap and delocalization of electrons in d-orbitals. In addition, the nephelauxetic ratio (β) was found to be less than one (0.71), denoting a partial covalent character for the σ bond created between the Co(II) ion and the chelating ligand.[65,66] The covalent property of this bond led to a decrease of the positive charge on the Co(II) ion due to the inductive effect of the ligand, which led to an increase in radial extension of d-orbitals and a decrease in electron–electron repulsion. By contrast, the $10D_q$ (8600 cm^{-1}), LFSE (191 cm^{-1}), ν_3/ν_1 (1.595), and ν_3/ν_2 (1.043) values are in agreement with those reported for high-spin octahedral cobalt(II) complex.[65]

3.6 | Thermal studies

The TG and DTA temperature ranges, the decomposition stages as well as the weight loss percentage of complexes are listed in Table 4. The TG data were recorded using 2–5 mg of samples at a constant heating rate of 10 °C/min under a nitrogen atmosphere using a thermal analyzer.

The thermal behavior of chloride complexes **1**, **4**, and **11** was investigated by TG analysis, with results presented in Scheme 4. The thermal degradation occurs in three major stages within temperature ranges 25–263 °C, 211–451 °C, and 343–772 °C. The first one refers to the desolvation stage, which does not point, in general, to a single event but rather to two overlapping events. The

TABLE 3 Electronic spectral data and magnetic moments of the **HL** ligand and its metal complexes

No.	Compound	Spectral bands (nm)	Assignment	$\mu_{eff.}$ (BM) per metal ion
	$H_2L{\cdot}H_2O$	256, 301	π–π*	–
		374		
		456	n–π*	
1	$[Co(HL)Cl(OH)]{\cdot}3.5H_2O$	246, 287	Intraligand transitions	4.82
		311, 432		
		470	LMCT	
		498	$^4A_2'(F) \rightarrow {}^4A_2'(P)$	
		632	$^4A_2'' (F) \rightarrow {}^4E''(P)$	
		695	$^4A_2'' (F) \rightarrow {}^4E' (F)$	
2	$[Co(HL)(OH)(H_2O)_2]NO_3{\cdot}1.75H_2O$	242,382	Intraligand transitions	5.10
		426	LMCT	
		502	$^4T_{1g}(F) \rightarrow {}^4T_{1g}(P)\ (\upsilon_3)$	
		524	$^4T_{1g}(F) \rightarrow {}^4A_{2g}(F)\ (\upsilon_2)$	
		801	$^4T_{1g}(F) \rightarrow {}^4T_{2g}(F)\ (\upsilon_1)$	
3	$[Co(HL)(OAc)(OH)]{\cdot}4.25H_2O{\cdot}0.25EtOH$	239, 333	Intraligand transitions	4.90
		350		
		502	$^4A_2'(F) \rightarrow {}^4A_2'(P)$	
		542	$^4A_2''(F) \rightarrow {}^4E''(P)$	
		751	$^4A_2''(F) \rightarrow {}^4E'(F)$	
4	$[Ni(HL)Cl]Cl{\cdot}4.5H_2O$	252, 351	Intraligand transitions	3.23
		386		
		405	LMCT	
		658	$^3T_1(F) \rightarrow {}^3A_2(F)$	
		795	$^3T_1(F) \rightarrow {}^3T_2(P)$	
		857	$^3T_1(F) \rightarrow {}^3T_2(F)$	
5	$[Ni(HL)(NO_3)_2]{\cdot}4.5H_2O$	247, 332	Intraligand transitions	3.36
		363		
		435	LMCT + $^2B_{1g} \rightarrow {}^2E_g$	
		664	$^2B_{1g} \rightarrow {}^2B_{2g}$	
		789	$^2B_{1g} \rightarrow {}^2A_{1g}$	
6	$[Ni(HL)(OAc)(OH)]{\cdot}4H_2O{\cdot}0.25EtOH$	249, 337	Intraligand transitions	3.52
		352		
		432	LMCT + $^2B_{1g} \rightarrow {}^2E_g$	
		622	$^2B_{1g} \rightarrow {}^2B_{2g}$	
		805	$^2B_{1g} \rightarrow {}^2A_{1g}$	
7	$[Cu(HL)(OH)(H_2O)_2]Cl{\cdot}4H_2O$	248, 350	Intraligand transitions	2.10
		384		
		395	LMCT	
		550	$^2B_{1g} \rightarrow {}^2E_g$	
		769	$^2B_{1g} \rightarrow {}^2B_{2g}$	
8	$[Cu(HL)(OH)(H_2O)_2]Br{\cdot}3.5H_2O{\cdot}0.25EtOH$	250, 345	Intraligand transitions	1.75
		359		

(Continues)

TABLE 3 (Continued)

No.	Compound	Spectral bands (nm)	Assignment	$\mu_{eff.}$ (BM) per metal ion
		540	$^2B_{1g} \rightarrow {}^2E_g$	
		760	$^2B_{1g} \rightarrow {}^2B_{2g}$	
		811	$^2B_{1g} \rightarrow {}^2A_g$	
9	$[Cu(L)(H_2O)]NO_3{\cdot}4.25H_2O$	246, 326	Intraligand transitions	1.81
		393		
		438	LMCT	
		502	$^2B_{1g} \rightarrow {}^2E_g$	
		665	$^2B_{1g} \rightarrow {}^2B_{2g}$	
10	$[Cu(HL)(OAc)(OH)]{\cdot}2.25H_2O$	254, 327	Intraligand transitions	1.85
		345		
		440	LMCT + $^2B_{1g} \rightarrow {}^2E_g$	
		690	$^2B_{1g} \rightarrow {}^2B_{2g}$	
		800	$^2B_{1g} \rightarrow {}^2A_{1g}$	
11	$[Zn(HL)Cl(OH)(H_2O)]{\cdot}6.5H_2O$	255	Intraligand transitions	Diamagnetic
		340		
		450	LMCT	
12	$[Cd(HL)(NO_3)_2(H_2O)]{\cdot}2.25H_2O{\cdot}0.25EtOH$	250	Intraligand transitions	Diamagnetic
		345		
		460	LMCT	

desolvation stage takes place within ranges 25–211 °C, 33–264 °C, and 31–233 °C attributable to removal of 3, 4.25, and 3.25 mol of water molecules of crystallization with weight losses of 9.96%, 12.64%, and 9.19% for complexes **1**, **4**, and **11**, respectively. This degradation step is confirmed by weak DTA peaks observed at T_{max} = 42 and 149; 73, 131, 190; and 50, 130, and 157 °C, respectively. Then, the desolvation stage is followed by the second one in the 211–451 °C range corresponding to the loss of chloride ion and along with the elimination of the remaining lattice water and two terminal methyl groups in the antipyrine moiety. This step is associated with endothermic peaks located at 347, 320, 297, 351, and 438 °C. Finally, the third decomposition stage between 343 and 772 °C refers to a single process which points to removal of the remaining lattice and coordinated water molecules as well as the elimination of the coordinated anions and the substituted 1,2,4-triazole ring. The residual part of the thermal decomposition is consistent with metal sulfide mixed with carbon.[26]

The SP Cu(II) complexes **7** and **8** are isothermal and isostructural. The thermal behavior of these complexes occurs in three decompositions stages within temperature ranges 23–259, 205–359, and 357–800 °C (Scheme 5). The first one is the desolvation step which is associated with weak-medium endothermic DTA peaks at T_{max} = 52, 165, and 59 and 164 °C attributed to loss of 3 mol of crystallized water and complete desolvation with weight losses of 8.71% and 11.27% for complexes **7** and **8**, respectively. The complexes lose their water below 200 °C due to hydration, showing that water/solvent molecules in the complexes are absorbed.[69] Afterward, the coordinated water, anion, and the ligand partially decomposed in the second stage, corresponding to weak–strong endothermic DTA peaks at T_{max} = 212, 298, and 327 °C, which point to the removal of coordinated H_2O, lattice H_2O, and ionized halogen, respectively, along with partial ligand pyrolysis (3-pyridyl-1,2.4-triazole, $C_7H_5N_4$; Table 4). Finally, complete ligand pyrolysis occurs in association with the removal of remaining lattice and coordinated water molecules together with the removal of coordinated OH, with weight losses of 32.98% and 41.03% for complexes **7** and **8**, respectively. This step ended with the formation of CuO (Table 4).[70,71] By contrast, the $CuBr_2$ complex showed a higher thermal stability than the $CuCl_2$ complex. This behavior can be interpreted based on nucleophilic power of the halide ion (electron-donor constants: Cl = 1.24 and Br = 1.51), which stabilizes the activated intermediate.[72]

The acetate complexes **3** and **6** thermally decompose in three degradation steps within temperature ranges 25–230 °C, 227–414 °C, and 397–850 °C. The first one corresponds to weight losses of 14.70% and 13.44% attributed to complete desolvation, which takes place in more

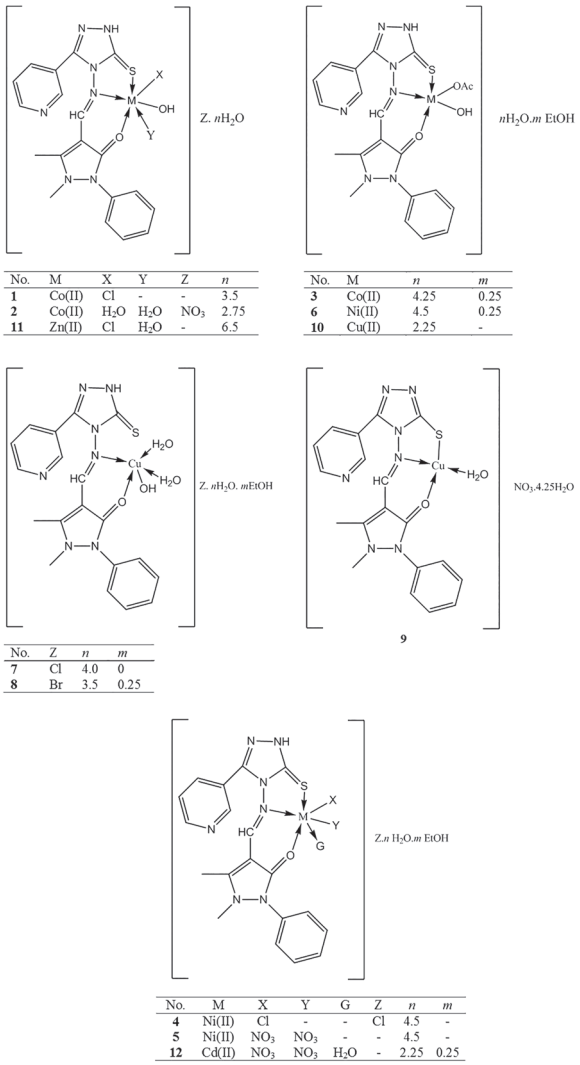

No.	M	X	Y	Z	n
1	Co(II)	Cl	-	-	3.5
2	Co(II)	H_2O	H_2O	NO_3	2.75
11	Zn(II)	Cl	H_2O	-	6.5

No.	M	n	m
3	Co(II)	4.25	0.25
6	Ni(II)	4.5	0.25
10	Cu(II)	2.25	-

No.	Z	n	m
7	Cl	4.0	0
8	Br	3.5	0.25

No.	M	X	Y	G	Z	n	m
4	Ni(II)	Cl	-	-	Cl	4.5	-
5	Ni(II)	NO_3	NO_3	-	-	4.5	-
12	Cd(II)	NO_3	NO_3	H_2O	-	2.25	0.25

FIGURE 2 Structure of complexes **1–12**

than one event for complex **3**. This is confirmed by weak/medium endothermic DTA peaks at T_{max} = 70 and 192, and 74 °C for complexes **3** and **6**, respectively. Afterward, the coordinated acetate ion and the ligand are partially decomposed (C_6H_5) in the second stage within temperature ranges 230–414 and 227–397 °C, which are associated with estimated weight losses of 22.07% and 23.14% for complexes **3** and **6**, respectively. This step is clarified by weak endothermic DTA peaks at T_{max} = 374 and 318 °C. Finally, complete decomposition of the compound with the elimination of the coordinated OH ion occurs in association with weight losses of 45.74% and 46.0% for complexes **3** and **6**, respectively. This step ended with the formation of metal oxide contaminated with carbon residues[20,49,70] as observed in Scheme 6 and Table 4.

The TG curve of complex Cu(HL)(OAc)(OH)]·2.25H_2O (**10**) shows three thermal decomposition stages between 26 and 600 °C. In the first stage, which occurs between 26 and 238 °C, the thermogram depicts a weight loss of 6.92%, which can be attributed to loss of 2.25 mol of crystallized water molecules. This event is associated with two weak endothermic peaks at T_{max} = 47 and 196 °C. Then, the anhydrous complex decomposes in two separate steps: the first one occurs between 238 and 349 °C with a weight loss of 33.77%, which can be attributed to loss of 1 mol of coordinated acetate ion, 1 mol of coordinated OH ion, and partial ligand degradation ($C_6H_4N_3$). This step is clarified by a weak exothermic DTA peak at T_{max} = 314 °C. Finally, the last step occurring between 349 and 600 °C denotes complete pyrolytic decomposition of the compound that produces a mixture of CuO and carbon as a final residue.[49,67,70] The thermal decomposition can be explained as follows :

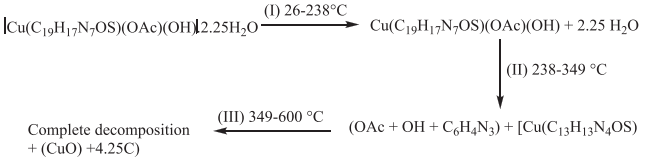

The TG curves of nitrato complexes **2**, **5**, and **12** reveal four decomposition steps within temperature ranges 23–234 °C, 195–320 °C, 300–566 °C, and 450–908 °C (Table 4). The first step is accompanied by estimated mass losses of 14%, 12.71%, and 7.35% attributable to partial desolvation together with removal of ionic nitrate for complex **2** and complete desolvation for complexes **5** and **12**, respectively. This step is associated with weak endothermic peaks appearing at 137 and 217 °C, 40 and 134 °C, and 100 °C for complexes **2**, **5**, and **12**, respectively. The DTA curves confirm that the surface water molecules adsorbed are lost up to 100 °C in these complexes, with endothermic peaks characterized for complexes **5** and **12**. Beyond this temperature, the complexes experience decomposition at 234, 216, 195 °C (Table 4), respectively. This represents the second step associated with mass loses of 15.08%, 18.38%, and 20.20% assignable to removal of coordinated water, hydroxyl, and coordinated nitrate ions, respectively, as well as partial ligand pyrolysis (C_2H_4) and elimination of remaining lattice water (complex **2**). This step is clarified by a medium exothermic DTA peak at 265 and 252 °C corresponding to removal of coordinated nitrate in complexes **5** and **12**, respectively.[73,74] The second step is followed by the subsequent elimination of the ligand in the third and fourth decomposition steps to obtain stable metal oxide at high temperatures contaminated with traces of carbon as the final product.[48,70,74] This is supported by endothermic and exothermic peaks through all decomposition stages.

TABLE 4 Thermal analyses (thermogravimetric/differential thermal analysis) data for Schiff base (**HL**) metal complexes

No.	Compound	Thermogravimetric temperature range (°C)	Differential thermal analysis peak (°C)	Mass loss (%)		Assignment	T_s
				Found	Calcd		
1	$[Co(HL)Cl(OH)]\cdot 3.5H_2O$	22–211	42(+)w, 149(+)w	9.96	9.55	Loss of 3 mol of crystallized H_2O[a]	211
		211–402	347(+)s	25.04	24.86	Loss of 0.5 mol of Cl_2 gas and partial ligand pyrolysis (C_6H_5+ C_2H_4)[d]	
		402–772	461(+)w, 497(+)mb, 719(+)m	49.95	49.52	Loss of 0.5 mol of lattice H_2O and 1 mol of coordinated OH and ligand pyrolysis ($C_{11}H_8N_7O$)[d]	
		At 772		15.46	16.07	(CoS)[f]	
2	$[Co(HL)(OH)(H_2O)_2]NO_3\cdot 1.75H_2O$	22–55	–	–	–	Stable zone	234
		55–234	137(+)m 217(+)w	14.00	14.16	Loss of 1.25 mol of crystallized H_2O and 1 mol of ionic nitrate[a]	
		234–315	–	15.08	15.10	Loss 2 mol of coordinated H_2O, OH, 0.5 mol of lattice H_2O, and ligand pyrolysis (C_2H_4)[d]	
		315–510	424(+)br 479(+)s	30.24	30.35	Partial ligand pyrolysis ($C_6H_3N_2$ and C_5H_4N)[d]	
		510–650	550(−)s	20.59	20.29	Complete ligand pyrolysis ($C_{2.25}H_6N_4S$)[d]	
		At 650		20.10	20.10	(CoO + 3.75C)[f]	
3	$[Co(HL)(OAc)(OH)]\cdot 4.25H_2O\cdot 0.25EtOH$	30–230	70(+)w, 192(+)w	14.70	14.34	Loss of 0.25 mol of EtOH and 4.25 mol of crystallized H_2O[a + b]	230
		230–414	374(+)w	22.07	22.16	Loss of 1 mol of coordinated acetate and C_6H_5 (partial ligand pyrolysis)[d]	
		414–850	463(+)w, 490(+)w, 691(+)s	45.74	45.94	Loss of 1 mol of coordinated OH and partial ligand pyrolysis ($C_{10.25}H_{12}N_7S$)[d]	
		At 850		17.50	17.56	(CoO + 2.75C)[f]	
4	$[Ni(HL)Cl]Cl\cdot 4.5H_2O$	33–263	73(+)w, 131(+)w, 190(−)m	12.64	12.72	Loss of 4.25 mol of crystallized H_2O[a]	263
		263–343	320(+)m	24.57	24.11	Loss of 1 mol of ionic chloride ion and 0.25 mol of lattice H_2O and ligand pyrolysis (C_6H_5 and C_2H_4)[d]	
		343–753	512(+)m, 613(+)mb, 757(+)w	47.56	48.11	Loss of 1 mol of coordinated chloride ion and ligand pyrolysis ($C_{11}H_8N_7O$)[d]	
		At 753		15.25	15.06	(NiS)[f]	
5	$[Ni(HL)(NO_3)_2]\cdot 4.5H_2O$	23–216	40(+)w, 134(+)w	12.71	12.38	Loss of 4.5 mol of crystallized H_2O[a]	216

(Continues)

TABLE 4 (Continued)

No.	Compound	Thermogravimetric temperature range (°C)	Differential thermal analysis peak (°C)	Mass loss (%)		Assignment	T_s
				Found	Calcd		
		216–320	265(−)m	18.38	18.93	Loss of 2 mol of coordinated nitrate[d]	
		320–450	421(−)m	39.48	38.96	Partial ligand pyrolysis (C_6H_5, $C_5H_4N_2$, and $C_3H_4N_2S$)	
		450–908	491(+)s, 834(−)s	15.91	16.04	Complete ligand pyrolysis ($C_{3.75}H_4N_4$)[d]	
		At 908		13.54	13.69	(NiO + 1.25C)[f]	
6	[Ni(HL)(OAc)(OH)]·4H_2O·0.25EtOH	25–227	74(+)s	13.44	13.71	Loss of 0.25 mol of EtOH and 4 mol of lattice H_2O[a + b]	227
		227–397	318(+)w	23.14	22.33	Loss of 1 mol of coordinated acetate and C_6H_5 (partial ligand pyrolysis)[d]	
		397–800	503(+)s, 650(+)mb	46.0	46.78	Loss of 1 mol of coordinated OH and complete ligand pyrolysis ($C_{10.5}H_{12}N_7S$)[d]	
		At 800		17.53	17.18	(NiO + 2.5C)[f]	
7	[Cu(HL)(OH)(H_2O)$_2$]Cl·4H_2O	25–205	52(+)w, 165(+)w	8.71	8.78	Loss of 3 mol of crystallized H_2O[a]	205
		205–357	212(+)w, 298(+)w	35.57	35.21	Loss of 1 mol of coordinated H_2O, 1 mol of lattice H_2O, 2 mol of ionic chloride, and $C_7H_5N_4$ (ligand pyrolysis)[d]	
		357–800	417(+)w, 571(+)m	32.98	33.34	Loss of 1 mol of coordinated H_2O, coordinated OH, and complete ligand pyrolysis ($C_7H_{12}N_3S$)[d]	
		At 800		22.75	22.67	(CuO + 5C)[f]	
8	[Cu(HL)(OH)(H_2O)$_2$]Br·3.5H_2O·0.25EtOH	23–259	59(+)m, 164(+)mb	11.27	11.26	Loss of 3.5 mol of crystallized H_2O and 0.25 mol of EtOH[a + b]	259
		259–359	327(+)s	35.92	36.70	Loss of 1 mol of coordinated H_2O, 1 mol of ionic bromide, and $C_7H_5N_4$ (ligand pyrolysis)[d]	
		359–750	670(+)mb	41.03	40.04	Loss of 1 mol of coordinated H_2O, OH, and ligand pyrolysis ($C_{12}H_{12}N_3S$)[d]	
		At 750		11.80	12.00	(CuO)[f]	
9	[Cu(L)(H_2O)]NO_3·4.25H_2O	22–219	79(+)w, 207(−)s	23.12	22.71	Loss of 4.25 mol of lattice H_2O and 1 mol of ionic NO_3[a]	219
		219–408	301(+)w	24.12	24.11	Partial ligand pyrolysis ($C_9H_{10}N_2$)[d]	

(Continues)

TABLE 4 (Continued)

No.	Compound	Thermogravimetric temperature range (°C)	Differential thermal analysis peak (°C)	Mass loss (%)		Assignment	T_s
				Found	Calcd		
		408–630	440(+)m, 550(−)m	37.50	37.54	Loss of 1 mol of coordinated H_2O and complete ligand pyrolysis ($C_{10}H_6N_5O$)[d]	
		At 630		15.28	15.64	(CuS)[f]	
10	[Cu(HL)(OAc)(OH)]·2.25H_2O	26–238	47(+)m, 196(+)m	6.92	7.09	Loss of 2.25 mol of lattice H_2O[a]	238
		238–349	314(−)m	33.77	33.98	Loss of coordinated CH_3COO, OH, and partial ligand pyrolysis ($C_6H_4N_3$)[d]	
		349–600	478(+)w, 513(+)m	36.15	36.08	Complete ligand pyrolysis ($C_{8.75}H_{13}N_4S$)[d]	
		At 600		23.18	22.85	(CuO + 4.25C)[f]	
11	[Zn(HL)Cl(OH)(H_2O)]·6.5H_2O	31–233	50(+)w, 130(+), 157(+)w	9.19	9.09	Loss of 3.25 mol of lattice H_2O[a]	233
		233–451	297(+)wb, 351(+)mb, 438(+)mb	24.09	24.62	Loss of 1 mol of lattice H_2O, 0.5 mol of coordinated Cl_2, and partial ligand pyrolysis (C_6H_5+ C_2H_4)[d]	
		451–720	610(−)b	47.86	47.45	Loss of 2.25 mol of lattice H_2O, 1 mol of coordinated H_2O and OH, and complete ligand pyrolysis ($C_9H_8N_7O$)[d]	
		At 720		18.87	18.84	(ZnS + 2C)[f]	
12	[Cd(HL)(NO_3)$_2$(H_2O)]·2.25H_2O·0.25EtOH	24–65		–	–	Stable zone	195
		65–195	100(+)w	7.35	7.46	Loss of 0.25 mol of EtOH and 2.25 mol of crystallized H_2O[a + b]	
		195–300	252(−)m	20.20	20.35	Loss of 2 mol of coordinated NO_3 and 1 mol of coordinated H_2O[d]	
		300–566	425(−)mb, 512(−)mb	26.02	25.97	Partial ligand pyrolysis (C_6H_5, C_5H_4N, and C_2H_2)[d]	
		566–800		27.64	27.82	Complete ligand pyrolysis ($C_6H_6N_6S$)[d]	
		At 800		18.70	18.40	(CdO)[f]	

Abbreviations: [a]dehydration; [b]desolvation; [d]decomposition; [f]final residue; b, broad; m, medium; s, strong; T_S, thermal stability; w, weak; +, endothermic peak; −, exothermic peak.

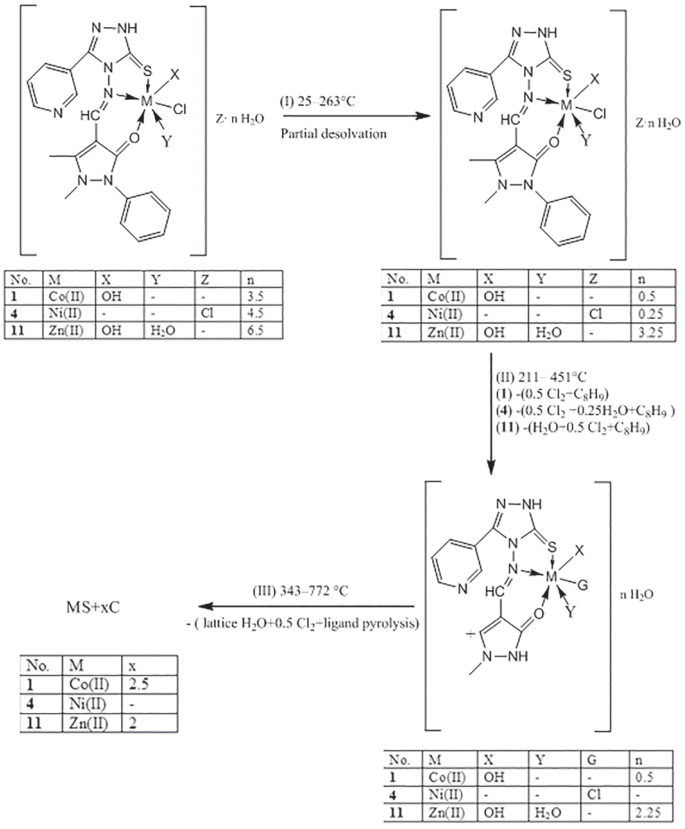

No.	M	X	Y	Z	n
1	Co(II)	OH	-	-	3.5
4	Ni(II)	-	-	Cl	4.5
11	Zn(II)	OH	H_2O	-	6.5

No.	M	X	Y	Z	n
1	Co(II)	OH	-	-	0.5
4	Ni(II)	-	-	Cl	0.25
11	Zn(II)	OH	H_2O	-	3.25

No.	M	X	Y	G	n
1	Co(II)	OH	-	-	0.5
4	Ni(II)	-	-	Cl	-
11	Zn(II)	OH	H_2O	-	2.25

No.	M	x
1	Co(II)	2.5
4	Ni(II)	-
11	Zn(II)	2

SCHEME 4 Thermal decomposition mechanism of complexes **1**, **4**, and **11**

SCHEME 5 Thermal decomposition mechanism of complexes **7** and **8**

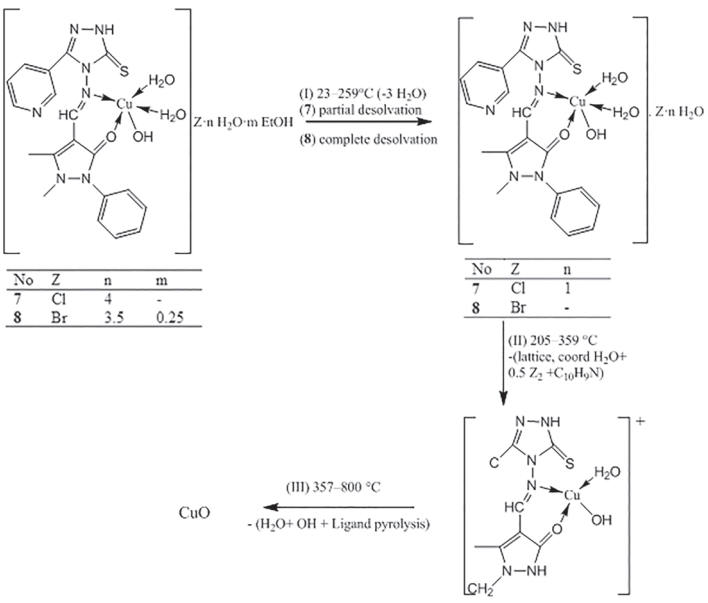

No	Z	n	m
7	Cl	4	-
8	Br	3.5	0.25

No	Z	n
7	Cl	1
8	Br	-

3.7 | ESR studies

The ESR spectra of complexes **7**, **8**, and **10** confirmed their electronic spectra which are consistent with distorted SP geometries. The polycrystalline ESR spectral parameters of copper(II) chelates are summarized in Table 5. This spectral strategy gives information about the binding mode around the copper(II) ion. In the solid state, the ESR spectra of copper(II) complexes **7**, **8**, and **10** at room temperature display distinctive types of symmetrical species. The ESR spectra of copper(II) complexes **7**, **8**, and **10** are shown in Figures S16–S18.

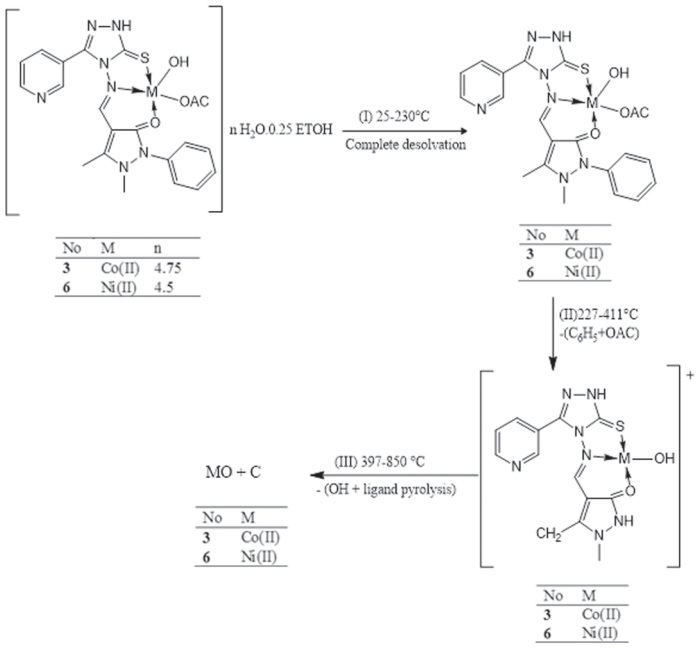

SCHEME 6 Thermal decomposition mechanism of complexes **3** and **6**

TABLE 5 Electron spin resonance bonding and reduction parameters for Cu(II) complexes

Complex	7	8	10
g_3	2.230	2.150	–
g_2	2.090	2.045	–
g_1	2.026	2.008	–
g_{av}[a]	2.115	2.068	–
$g_{\|\|}$	–	–	2.18
$g_\perp$	–	–	2.03
g_{iso}[b]	–	–	2.08
G[c]	4.28	6.13	6.56
R[d]	0.457	0.352	–
$A_{\|\|}$[c]	–	–	178.08
$A_\perp$[c]	–	–	23.69
Δ_1[f]	–	–	12,500
Δ_2[f]	–	–	15,385
α^2	–	–	0.72
$K_{\|\|}$	–	–	0.58
$K_\perp$	–	–	0.50
K[d]	–	–	0.53
β_1^2	–	–	0.46
γ_1^2	–	–	0.35
f[h]	–	–	122.41
Ground state	$^2B_{1g}$	$^2B_{1g}$	$^2B_{1g}$

[a]$g_{av} = g_1 + g_2 + g_3/3$,[c]$G = g_{||} - 2.0023/g_\perp - 2.0023$.
[b]$g_{iso} = 2g_\perp + g_{||}/3$,[d]$R = (g_2 - g_1)/(g_3 - g_2)$.
[c]A in 10^{-4} cm^{-1},[f]Δ in cm^{-1}.
[d]$K = 2K_\perp + K_{||}/3$,[h]$f = g_{||}/A_{||}$ in centimeter.

The X-band ESR spectra of complexes **7** and **8** give three g values, $g_1 = 2.026$ and 2.008, $g_2 = 2.090$ and 2.045, and $g_3 = 2.23$ and 2.15, with g_{av} value of 2.115 and 2.068 (Table 5), respectively, affording rhombic distortion in the coordination sphere.[64,75] The spectra with three g values are clearly indicative of a penta-coordinated Cu(II) complex with a geometrical TBP or the SP structure. The geometric parameter (R) has been calculated using this ratio $R = (g_2 - g_1)/(g_3 - g_2)$ to set up the ground state.[64,75] If $R > 1$, $(d_z^2)^1$ represents the ground state in the TBP geometrical structure, whereas if $R < 1$, the ground term has a $(d_{x^2-y^2})^1$ configuration in the SP structure. For the Cu(II) complexes **7** and **8** R values are 0.457 and 0.352, suggesting the existence of the unpaired electron in $(d_{x^2-y^2})$, giving $(^2B_{1g})$ as the ground state with configuration $(e_g)^4(b_{2g})^2(a_{1g})^2(b_{1g})^1$, which is characterized as SP Cu(II) complexes.

By contrast, the spectrum of complex **10** displays broad signal with two g values and an axial-type ESR signal with $g_\perp = 2.03$ and $g_{||} = 2.18$ (g_{iso} value is 2.08). This change in the g_{av} value suggests axial symmetry.[46,49,64] In addition, the observed $g_{||}$ is less than 2.3, pointing to the covalent nature of the copper-ligand bond. According to Hathaway and Billing,[76] the parameter $G = (g_{||}-2)/(g_\perp-2)$ is used to measure the exchange interaction between copper centers in polycrystalline solids. In complexes **7**, **8**, and **10**, the G parameter is equal to 4.28–6.56, indicating the absence of exchange interaction between copper centers. The ESR spectra of $Cu(OAc)_2$ complex **10** presented a well-defined hyperfine structure at the lower field than that observed within the high field region ($A_{||} = 178.08$ and $A_\perp = 23.69 \times 10^{-4}$ cm^{-1}). This is due to weak interaction between electron spin and nuclear spin of the Cu(II) ion ($I = 3/2$). The empirical factor ($f = g_{||}/A_{||}$) can be used for diagnosing the stereochemistry of copper(II) complexes.[44,46] For the investigated complex, the f value was 122 cm, indicating tetragonal distorted copper(II) complex.[76] The interaction of the unpaired electron residues in the $(3d_{x^2-y^2})^1$ orbital (antibonding orbital) of the Cu(II) ion with the **σ** orbitals of the ligand is considered in the following equation:

$$\alpha^2 = A/0.036 + \left(g_{||} - g_e\right) + 3(g_\perp - g_e)/7 + 0.04$$

where the α^2 value measures the covalent nature of M–L bonding (i.e. the in-plane σ-bonding). The calculated in-plane σ-covalence parameter (α^2) value of 0.72 for complex **10** clarifies that this complex has more covalent character for σ-bonding. The bonding parameters (β^2) and (γ^2), which measure the covalence of in-plane and out-of-plane (π) bonding, respectively, can be calculated using ESR parameters $g_{||}$, $A_{||}$, $g_\perp$, $A_\perp$, and the energies of the d–d electronic transitions (Δ_1, Δ_2). The orbital reduction factors ($K^2_{||}$ and $K^2_\perp$) can be calculated using the following relations:

$$(\alpha^2\beta^2) = K^2_{||} = \left(g_{||} - 2.0023\right)\Delta_1/8\lambda_\circ \text{ and } (\alpha^2\gamma^2) = K^2_\perp = (g_\perp - 2.0023)\Delta_2/2\lambda^{[46,76]}$$

where $K_{||}$, $K_\perp$, $\lambda_\circ$, Δ_1, and Δ_2 are parallel and perpendicular orbital reduction factors; the spin-orbit coupling constant, which is −828 cm^{-1} for the Cu(II) ion; $^2B_{1g} \rightarrow {}^2B_{2g}$; and $^2B_{1g} \rightarrow {}^2E_g$, respectively. The nature of metal–ligand bonding can be elucidated and clarified using these factors. According to Hathaway and Billing,[76] $K_{||}K_{\perp z}$ and $K < 1$ imply the presence of out-of-plane π-bonding and covalent nature of M–L bonds. Moreover, the α^2, β^2, and γ^2 values are less than unit, which is attributed to significant in-plane σ-bonding and in-plane π-bonding.

3.8 | DFT studies

Because of our unsuccessful trials to obtain crystalline samples for X-ray crystallography, DFT calculations were performed to better understand the structures of the ligand and complexes **1**, **4**, **7**, **8**, and **9**. The optimized structures of **HL** ligand and its complexes are presented in Figure 3. No imaginary frequencies were recorded, which indicates that the investigated systems represent minima on their potential energy surface.

3.8.1 | Structure of the ligand

The calculations in the gas phase for the ligand indicated that the thione form (**HL**) is more stable than the thiol form (**HL′**) by 27 kcal/mol. Selected geometrical parameters for the ligand **HL** are shown in Tables 6 and 7. To shed light into the electronic structures of the ligand and its complexes, the natural bond orbital analysis was carried out. Charges from natural population analysis over some atoms in the ligand and its complexes are listed in Table 8. The negative charge on the oxygen atom O1 (−0.531) is larger than that for the nitrogen atoms N2 and N5 (−0.254 and −0.253, respectively), whereas both oxygen and nitrogen atoms are more negative than the sulfur atom (−0.220). Therefore, it is expected that the metal ion will preferably bind with the oxygen atom than with the nitrogen and sulfur atoms.

To further understand the interaction between the ligand and the metal ion, the FMOs are calculated as depicted in Figure 4. HOMO is the highest energy orbital containing electrons and is closely related to reactivity toward electrophilic attack, whereas LUMO is the lowest

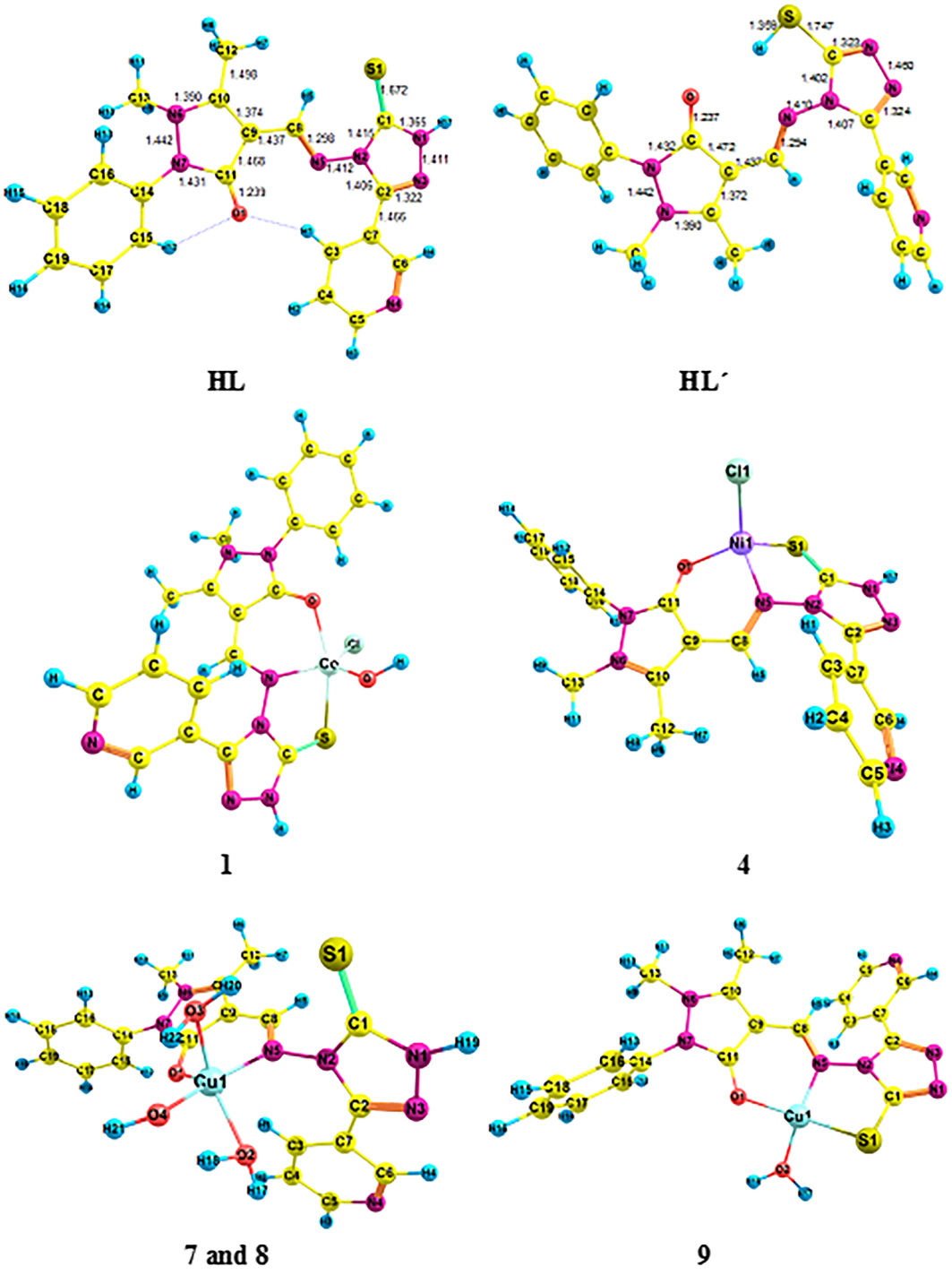

FIGURE 3 Optimized structures of the complexes, the ligand (**HL**), and its tautomer (**HL′**)

energy orbital that can accept electrons and correlates well with reactivity toward nucleophilic attack. The HOMO of the ligand **HL** is mainly located on oxygen, nitrogen, and sulfur atoms, implying that these are the centers ready for electron donation to electron-deficient metal ions. Moreover, the HOMO–LUMO energy gap reflects the chemical activity of the molecule and serves as a simple measure of its kinetic stability. The HOMO–LUMO gap represents the chemical hardness of the molecule as reported by Pearson.[77] The chemical hardness is defined as the resistance toward deformation or polarization of the electron cloud of the molecules[78] which implies an increase in the molecular stability with hardness. From the data of the HOMO and LUMO energies, the parameters that indicate the stability/reactivity/sensitivity such as energy gap, **ΔE**;

TABLE 6 Selected bond lengths (B,) for the studied complexes

	M–O1	M–N5	M–S1	M–O(H_2O)	M–Cl	M–O (OH)	M–O (NO_3)
1	2.03	1.92	2.69	1.78	2.29		
4	1.92	1.91	2.40		2.13		
7	1.97	1.91		1.94		1.917	
				1.92			
9	1.868	1.863	2.21	1.88			

TABLE 7 Selected bond angles (°) for the studied complexes

	O1–M–Cl	O1–M–N5	N5–M–S1	S1–M–Cl	O1–M–O2	S1–M–O1	S1–M–O2	S1–M–O2
1	85.16	88.60	79.84	86.28	103.74	106.81	99.53	123.30
4	112.98	93.66	86.81	114.41	–	121.51	–	–
7	–	92.80	–		123.05			
9	–	97.40	93.12	–	94.61	145.51	98.13	

TABLE 8 NBA charges of the ligand and the studied complexes at B3LYP/3-21G(d)

Atom/compound	HL	1	4	7 and 8	9
O1	−0.531	−0.561	−0.597	−0.569	−0.597
N5	−0.253	−0.411	−0.363	−0.384	−0.363
S1	−0.220	−0.078	−0.054	−0.201	−0.181
M		0.817	0.892	0.933	0.893

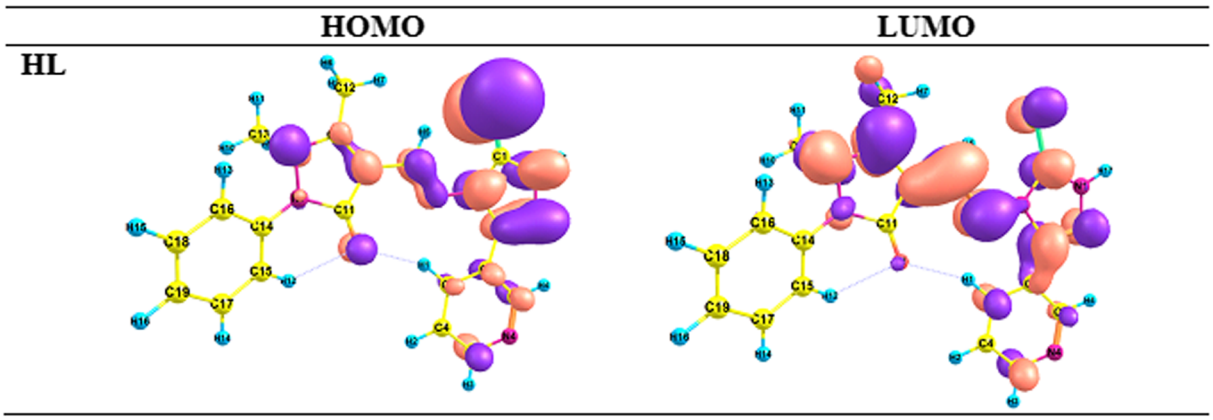

FIGURE 4 Density functional theory-computed highest occupied molecular orbital (HOMO) and lowest unoccupied molecular orbital (LUMO) diagrams of the ligand (**HL**)

absolute electronegativity, **χ**; chemical potentials, **Pi**; absolute hardness, **η**; absolute softness, **σ**; global electrophilicity, **ω**; global softness, **S**; and additional electronic charge, $\mathbf{\Delta N_{max}}$ have been calculated and presented in Table 9.

From the theoretical calculations, it was concluded that the free ligand is soft and reactive toward forming complexes with metal ions due to the small HOMO–LUMO energy gap (3.85 eV) and it has high biological activity due to the high **ω** value.

3.8.2 | Structure of the complexes

Complex **1** presents a TBP structure with the Co(II) ion coordinated to one azomethine nitrogen atom (N5),

TABLE 9 Various quantum chemical parameters of free ligand (HL) and its complexes

E (a.u.)	HL	1	4	7 and 8	9
Dipole moment (D)	8.75	11.16	13.09	11.50	19.80
E_{HOMO} (eV)	−5.65	−4.17	−8.66	−8.27	−8.26
E_{LUMO} (eV)	−1.79	−2.30	−5.68	−5.20	−5.53
ΔE (eV)	3.85	1.86	2.98	3.07	2.73
χ (eV)	3.72	3.23	7.17	6.73	6.89
η (eV)	1.925	0.935	1.490	1.535	1.38
σ (eV^{-1})	0.519	1.069	0.671	0.651	0.724
Pi (eV)	−3.72	−3.235	−7.17	−6.73	−6.89
S (eV^{-1})	0.259	0.534	0.335	0.325	0.362
ω (eV)	3.594	5.596	17.25	14.75	17.20
ΔN_{max}	−1.932	3.459	4.812	4.384	4.99

Abbreviations: HOMO, highest occupied molecular orbital; LUMO, lowest unoccupied molecular orbital.

oxygen atom of the OH^- group, and chloride ion. These three atoms form a distorted plane with the carbonyl oxygen atom (O1) and the thione sulfur atom coordinated to the Co(II) ion in the *z* axis, forming a TBP structure. Complexes **7** and **8** adopt an SP structure with the Cu(II) ion coordinated to one azomethine nitrogen atom, one oxygen of the OH^- group, and two oxygen atoms of two water molecules. These four atoms form a distorted plane with the carbonyl oxygen atom of the ligand (O1) coordinated to the Cu(II) ion in the *z* axis. Starting the optimization process with a regular octahedral structure for complexes **7** and **8**, where the ligand coordinated to the Cu(II) ion in the tridentate mode through the carbonyl oxygen atom, nitrogen and sulfur lead gradually to the distorted SP structure, where the sulfur atom leaves the coordination sphere. All these observations support the experimental results of the distorted SP structure for complexes **7** and **8**. There are two common structures for a five-coordinated Cu(II) center, SP or TBP geometry, which can be evaluated by the angular structural parameter ($\boldsymbol{\tau}$). $\boldsymbol{\tau}$ is defined as $[(\theta - \Phi)/60]$, where θ and Φ are the two largest coordination angles. It was reported that $\boldsymbol{\tau = 0}$ for a perfect SP and $\boldsymbol{\tau = 1}$ for ideal TBP.[79] The calculated $\boldsymbol{\tau}$ values of complexes **1** and **7** and **8** are 0.520° and 0.451°, respectively, which confirmed the distorted TBP geometry for the cobalt(II) ion and distorted SP geometry for the copper(II) ion. Moreover, the sum of the bond angles around Co(II) and Cu(II) is 340° and 339°, which implies a pyramidization degree of 20° and 21° for complexes **1** and **7** and **8**, respectively.

Complexes **4** and **9** have a tetrahedral structure and a square planar geometry, respectively, where the ligand coordinated in a tridentate mode with the metal center through azomethine nitrogen, oxygen, and sulfur atoms (one each). The calculated binding energies of the complexes in the gas phase are given in Table 10. The negative sign of the binding energies indicates that the investigated complexation reactions are thermodynamically favored. Although the oxygen atom O1 carries the highest negative charge in the ligand than the nitrogen and sulfur atoms, the calculations showed that the M–N5 bond length is the shortest compared with M–O1 and M–S1 bond distances. The smaller M–N bond length may be attributed to back donation between metal center and ligand nitrogen atom (N5), which leads to the significant increase in the negative charge of N5 in the complexes than in the ligand as shown in Table 7. It is known that the bond length between the metal atom and the ligand is shortened considerably due to the multiple-bond character produced by back donation.[80] By contrast, the negative charge on S decreases largely in complexes **1**, **4**, and **9** relative to the free ligand with the M–S bond lengths

TABLE 10 Calculated binding energies (kcal/mol) for the studied complexes in the gas phase

Compound	ΔE_0	ΔE_{298}	ΔH_{298}	ΔG_{298}
1	−1549.26	−1549.03	−1550.81	−1523.92
4	−995.214	−994.778	−995.963	−979.865
7	−1098.97	−1100.37	−1102.74	−1062.05
9	−253.663	−254.037	−255.222	−235.444

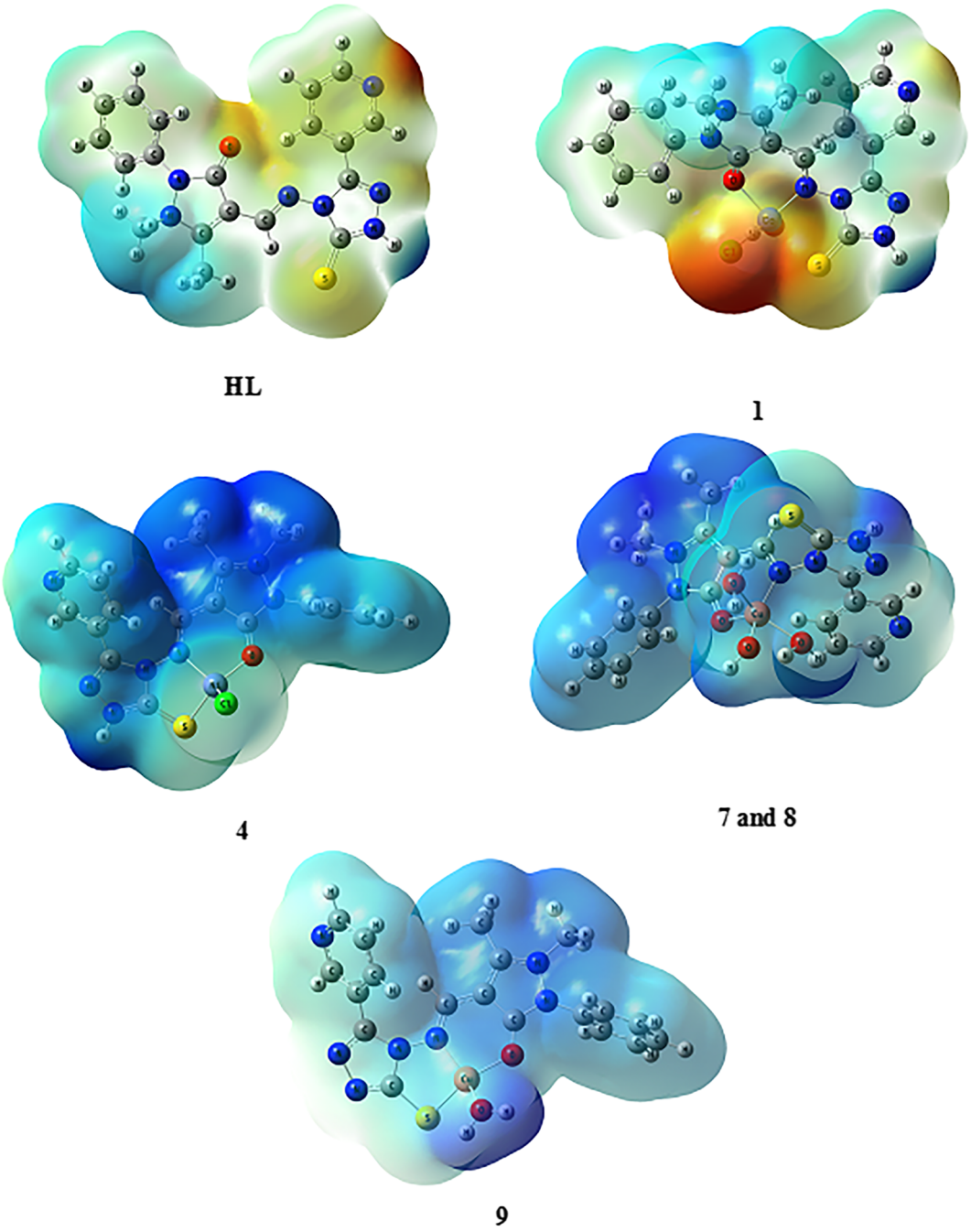

FIGURE 5 Molecular electrostatic potential (MEP) mapped on the electron density surface calculated by the DFT/B3LYP method for the ligand and its studied complexes. DFT, density functional theory

being the longest compared with the M–N and M–O bonds, which highlights their weaker nature. In addition, the ligand binds with the Cu(II) ion in complexes **7** and **8** as a bidentate ligand coordinated through N5 and O1, whereas the sulfur did not participate in coordination, which may be attributed to the weakness of the M–S bond. Besides, the charge on the metal ion in the complexes is less than +1 e, which indicates charge transfer from the ligands to the central metal ion. The dipole moments (D) for the complexes range from 11.16 to 19.8 Debye (Table 8), implying that all the complexes are highly polar compounds.

Regarding HOMO and LUMO energies in the free ligand and complexes, it is evident that the HOMO level in complexes **4, 7,** and **9** is stabilized by about 2.74 eV relative to ligand, whereas the LUMO is stabilized by about 3.74 eV compared with the ligand, which causes a decrease in energy gap in these complexes. In complex **1**, the HOMO is destabilized by 1.48 eV, whereas the LUMO is stabilized by 0.61 eV, which leads to a significant

TABLE 11 Antimicrobial activity of the **HL** ligand and its metal complexes

	Streptococcus pyogenes			*Escherichia coli*		
Compound	**100 ppm**	**200 ppm**	**500 ppm**	**100 ppm**	**200 ppm**	**500 ppm**
HL	30.0	60.0	100.0	20.0	50.0	100.0
1	40.0	75.0	160.0	50.0	90.0	160.0
2	40.0	90.0	140.0	30.0	70.0	100.0
4	50.0	80.0	150.0	60.0	100.0	220.0
5	40.0	70.0	120.0	31.0	70.0	120.0
11	60.0	120.0	230.0	60.0	110.0	240.0
12	70.0	120.0	250.0	80.0	150.0	250.0

reduction in the energy gap to 1.86 eV. The low energy gap ($\Delta E = E_{LUMO} - E_{HOMO}$) of the complexes than that of the ligand suggests a strong activity of the former (Table 9). The HOMO and LUMO diagrams of the complexes are shown in Figure S19.

MEP is suitable for predicting the reactive sites toward electrophilic and nucleophilic attack. The MEP of the ligand (**HL**) and the complexes is shown in Figure 5. The red and yellow regions (negative sites) of the MEP are related to electrophilic reactivity and the blue regions (positive sites) are related to nucleophilic reactivity. It can be seen from Figure 5 that the negative MEP regions of the ligand are concentrated on the carbonyl oxygen atom, azomethine nitrogen atom, and sulfur atom in addition to the pyridine nitrogen atom. Coordination of the ligand to the metal ion shifts the electrostatic potential to more positive values, which matches the higher global electrophilicity (**ω**) of the complexes compared with the ligand. The electrophilicity represents a suitable descriptor of the biological activity as there is a linear correlation between the electrophilicity and the biological activity of molecules,[81] which indicates a higher biological activity of the studied complexes compared with the ligand.

3.9 | Antibacterial studies

The bactericidal activities of Schiff base (**HL**) and its metal complexes **1**, **2**, **4**, **5**, **11**, and **12** were investigated using the agar plate technique on pathogenic bacteria and the data are listed in Table 11. The listed results show that the **HL** ligand has moderate sensitivity toward *S. pyogenes* than *E. coli*. Besides, metal complexes are observed to inhibit the investigated bacteria at different rates. These results revealed that the metal complexes have good inhibitory zones ranging from 7.0 to 25.0 mm for *S. pyogenes* (Gram positive). The biological activity has the following order: (**12**) (**11**) (**1**) (**4**) (**2**) (**5**). Moreover, the metal complexes have activity against *E. coli* (Gram negative) with inhibitory zone range of 5.0–25.0 mm. The order of biological activity is as follows: (**12**) (**11**) (**4**) (**1**) (**5**) (**2**). The variation in the activity of different complexes against investigated organisms depends on the impermeability of microbial cells. The better activity of metal complexes can be demonstrated on the basis of Overtone's concept and Tweedy's chelation theory.[82] Upon complexation, the polarity of the central metal atom is reduced, due to the partial sharing of its positive charge with the donor sites within the complex. This process causes an increase in the lipophilic nature of the metal, favoring its permeation through lipid layers of the microorganism to be destroyed.[83]

4 | CONCLUSIONS

In this paper, Co(II), Ni(II), Cu(II), Zn(II), and Cd(II) complexes with Schiff base ligand bearing 3-(3′-pyridyl)-4-amino-5-mercapto-1,2,4-triazole were synthesized. The investigated compounds were fully characterized using spectral methods and thermal and magnetic studies. Based on spectral results, octahedral geometries were suggested for complexes **2**, **11**, and **12**, and SP geometries for **5–8** and **10**. By contrast, complexes **1** and **3**, **4**, and **9** adopt a TBP, tetrahedral, and square planar geometrical structure, respectively. The ligand acts as a neutral and monobasic tridentate moiety, and coordinates to the metal ion through NOS donors in complexes **1–6**, **10–12**, and (**9**), respectively. By contrast, in complexes **7** and **8** the ligand behaves as a neutral bidentate, chelating to the Cu(II) ion though NO donors.

The ESR spectrum of copper(II) complex **10** is axial in nature with hyperfine splitting with $^2B_{1g}$ as a ground state. Complexes **7** and **8** undergo distortion around the Cu(II) center affording rhombic ESR spectra. The thermal studies revealed different types of crystallized solvents attached to the chelates. DFT calculations support the

experimental characterization of the ligand structure and its complexes. The antimicrobial screening assay of the compounds revealed higher activity of the metal complexes than the ligand (**HL**) toward *S. pyogenes* and *E. coli.*

ORCID

Dina A. Tolan https://orcid.org/0000-0003-3917-2822
Ahmed M. El-Nahas https://orcid.org/0000-0002-8547-7574

REFERENCES

[1] S. Banerjee, S. Ganguly, K. K. Sen, *J. Adv. Pharm. Edu. Res.* **2013**, *3*, 102.
[2] S. U. Cicekli, T. Onkol, S. Ozgen, M. F. Sahin, *Rev. Roum. Chim.* **2012**, *57*, 187.
[3] A. M. Hammam, M. A. EL-Gahami, Z. A. Khafagi, M. S. AL-Sadimi, S. A. Ibrahim, *J. Mater. Environ. Sci.* **2015**, *6*, 1596.
[4] H. Khanmohammadi, M. H. Abnosib, A. Hosseinzadeh, M. Erfantalab, *Spectrochim. Acta A* **2008**, *71*, 1474.
[5] V. Reddy, N. Patil, T. Reddy, S. D. Angadi, *Oriental J. Chem.* **2008**, *24*, 201.
[6] H. Khanmohammadi, M. Erfantalab, G. Azimi, *Spectrochim. Acta A* **2013**, *105*, 338.
[7] S. A. Patil, M. Manjunatha, A. D. Kulkarni, P. S. Badami, *Complex Metals* **2014**, *1*, 128.
[8] P. G. Avajiy, S. A. Patil, P. S. Badami, *J. Coord. Chem.* **2008**, *61*, 1884.
[9] V. Reddy, N. Patil, T. Reddy, S. D. Angadi, *E J. Chem.* **2006**, *5*, 529.
[10] K. Singh, Y. Kumar, P. Puri, C. Sharma, K. R. Aneja, *Phosphorus, Sulfur Silicon Relat. Elem.* **2012**, *187*, 1498.
[11] B. Namratha, L. Santosh, *Gaonkar, Int. J. Pharm. Pharm. Sci.* **2014**, *6*, 73.
[12] I. M. El-Deen, A. F. Shoair, M. A. El-Bindary, *J. Mol. Liq.* **2018**, *249*, 533.
[13] S. El-Metwally, A. K. Khalil, *Acta Chim. Slov.* **2010**, *57*, 941.
[14] A. M. Farghaly, A. A. Hozzaa, M. S. Abouzeit-Har, F. M. Sharabi, *Pharmazie* **1980**, *35*, 596.
[15] S. Manfredini, C. B. Vicentini, M. Manfrini, N. Bianchi, C. Rutigliano, C. Mischiati, R. Gambari, *Bioorg. Med. Chem.* **2000**, *8*, 2343.
[16] Y. Li, Y. Liu, H. Wang, X. Xiong, P. Wei, F. Li, *Molecules* **2013**, *18*, 877.
[17] T. Rosu, S. Pasculescu, V. Lazar, C. Chifiriuc, R. Cernat, *Molecules* **2006**, *11*, 904.
[18] G. Turhan-Zitouni, M. Sivaci, F. S. Kilic, K. Erol, *Eur. J. Med. Chem.* **2001**, *36*, 685.
[19] M. Manjunath, A. D. Kulkarni, G. B. Bagihalli, S. Malladi, S. A. Patil, *J. Mol. Struct.* **2017**, *1127*, 314.
[20] S. M. Emam, S. A. Abouel-Enein, F. I. Abouzayed, *Appl. Organomet. Chem.* **2017**, *4073*, 1.
[21] S. Chandra, L. K. Gupta, *Spectrochim. Acta A* **2005**, *61*, 269.
[22] R. J. R. Sorenson (Ed), *Biology of Copper Complexes*, Human Press, Clifton, NJ **1987**.
[23] J. Joseph, K. Nagashri, G. A. B. Rani, J. Saudi, *Chem. Soc.* **2013**, *17*, 285.
[24] R. Zhang, Q. Wang, Q. Li, C. Maa, *Inorg. Chim. Acta* **2009**, *362*, 2762.
[25] A. K. Singh, O. P. Pandey, S. K. Sengupta, *Spectrochim. Acta A* **2012**, *85*, 1.
[26] K. Singh, M. S. Barwa, P. Tyagi, *Eur. J. Med. Chem.* **2006**, *41*, 147.
[27] G. B. Bagihalli, P. G. Avaji, S. A. Patil, P. S. Badami, *Eur. J. Med. Chem.* **2008**, *43*, 2639.
[28] K. Singh, Y. Kumar, P. Puri, M. Kumar, C. Sharma, *Eur. J. Med. Chem.* **2012**, *52*, 313.
[29] J. Bassett, R. C. Denney, G. H. Jeffery, J. Mendham, *Vogel's Textbook of Quantitative Inorganic Analysis Including Elementary Instrumental Analysis*, 4th ed., Longman Group, London **1978**.
[30] J. Lewis, R. G. Wilkins, *Modern Coordination Chemistry*, Interscience, New York **1960** 403.
[31] P. Tgagi, S. Chandra, B. S. Saraswat, D. Yadav, *Spectrochim. Acta A* **2015**, *145*, 155.
[32] Y. Zasshi, *J. Pharm. Soc. Japan* **1956**, *76*, 167.
[33] S. O. Oyedemi, A. J. Afolayan, *Asian Pac. J. Trop. Med.* **2011**, *4*, 952.
[34] A. A. Abdulkarem, *J. Biophys. Chem.* **2017**, *8*, 13.
[35] I. P. Ejidike, P. A. Ajibade, *Bioinorg. Chem. Appl.* **2015**, *2015*, 1.
[36] R. G. Parr, W. Yang, *Density-Functional Theory of Atoms and Molecules*, Oxford University Press, New York, Oxford **1989**.
[37] T. Ziegler, *Chem. Rev.* **1991**, *91*, 651.
[38] M. J. Frisch, G. W. Trucks, H. B. Schlegel, G. E. Scuseria, M. A. Robb, J. R. Cheeseman, V. G. Zakrzewski, J. A. Montgomery Jr., R. E. Stratmann, J. C. Burant, S. Dapprich, J. M. Millam, A. D. Daniels, K. N. Kudin, M. C. Strain, O. Farkas, J. Tomasi, V. Barone, M. Cossi, R. Cammi, B. Mennucci, C. Pomelli, C. Adamo, S. Clifford, J. Ochterski, G. A. Petersson, P. Y. Ayala, Q. Cui, K. Morokuma, P. Salvador, J. J. Dannenberg, D. K. Malick, A. D. Rabuck, K. Raghavachari, J. B. Foresman, J. Cioslowski, J. V. Ortiz, A. G. Baboul, B. B. Stefanov, G. Liu, A. Liashenko, P. Piskorz, I. Komaromi, R. Gomperts, R. L. Martin, D. J. Fox, T. Keith, M. A. Al-Laham, C. Y. Peng, A. Nanayakkara, M. Challacombe, P. M. W. Gill, B. Johnson, W. Chen, M. W. Wong, J. L. Andres, C. Gonzalez, M. Head-Gordon, E. S. Replogle, J. A. Pople, *Gaussian 98*, Gaussian, Inc, Pittsburgh, PA **1998**.
[39] A. D. Becke, *J. Chem. Phys.* **1993**, *98*, 5648.
[40] C. Lee, W. Yang, R. G. Parr, *Phys. Rev.* **1988**, *37*, 785.
[41] P. J. Stephens, F. J. Devlin, C. Chabalowski, M. J. Frisch, *J. Phys. Chem.* **1994**, *98*, 11623.
[42] G. A. Zhurko, D. A. Zhurko, ChemCraft version 1.7 (build 132), http://www.chemcraftprog.com.
[43] S. Saikat, N. S. Kumar, C. A. Prasun, D. Kamalendu, *Ind. J. Sci.* **2015**, *12*, 17.
[44] S. A. AbouEl-Enein, S. M. Emam, M. W. Polis, E. M. Emara, *J. Mol. Struct.* **2015**, *1099*, 567.
[45] I. Ledeti, A. Alexa, V. Bercean, G. Vlase, T. Vlase, L.-M. Suta, A. Fulias, *Int. J. Mol. Sci.* **2015**, *16*, 1711.
[46] S. M. Emam, I. E.-T. El Sayed, M. I. Ayad, H. M. R. Hathout, *J. Mol. Struct.* **2017**, *1146*, 600.
[47] N. Upmanyu, J. K. Gupta, K. Shah, P. Mishra, *J. Pharm. Bioallied Sci.* **2011**, *3*, 259.

[48] S. M. Emam, S. A. AbouEl-Enein, E. M. Emara, *J. Therm. Anal. Calorim.* **2017**, *127*, 1611.
[49] S. M. Emam, S. A. AbouEl-Enein, E. M. Abdel-Satar, *Appl. Organomet. Chem.* **2019**, *33*, 1.
[50] A. Jha, Y. Murty, G. Durga, *Res. J. Pharm. Bio. Chem. Sci.* **2015**, *6*, 1306.
[51] R. D. Hunashal, P. M. Ronad, V. S. Maddi, D. Satyanarayana, M. A. Kamadod, *Arabian J. Chem.* **2014**, *7*, 1070.
[52] R. V. Gadag, M. R. Gajendragad, *Talanta* **1978**, *25*, 418.
[53] C. N. R. Rao, R. Venkataraghavan, T. R. Kasturi, *Can. J. Chem.* **1964**, *42*, 36.
[54] X.-X. Ye, Z.-F. Chen, A.-J. Zhang, L.-X. Zhang, *Molecules* **2007**, *12*, 1202.
[55] K. Singh, P. Puri, Y. Kumar, C. Sharma, K. R. Aneja, *Bioinorg. Chem. Appl.* **2011**, *2011*, 1.
[56] A. Szorcsik, L. Nagy, J. Sletten, G. Szalontai, E. Kamu, T. Fiore, L. Pellerito, E. Kalman, *J. Organomet. Chem.* **2004**, *689*, 1145.
[57] V. C. Wei, L. Y. Tuan, L. D. Zheng, *Chin. J. Chem.* **2000**, *18*, 351.
[58] B. S. Grag, D. N. Kumar, M. Sarbhai, *Spectrochim. Acta A* **2005**, *61*, 141.
[59] M. S. Nair, R. S. Joseyphus, *Spectrochim. Acta A* **2008**, *70*, 749.
[60] V. P. Singh, *Spectrochim. Acta A* **2008**, *71*, 17.
[61] H. A. Sahyon, A. A. El-Bindary, A. F. Shoair, A. A. Abdellatif, *J. Mol. Liq.* **2018**, *255*, 122.
[62] R. K. Dani, M. K. Bharty, S. Paswan, S. Singh, N. K. Singh, *Inorg. Chim. Acta* **2014**, *421*, 519.
[63] R. K. Mali, R. R. Somani, M. P. Toraskar, K. K. Mali, P. P. Naik, P. Y. Shirodkar, *Inter. J. Chem. Tech Res.* **2009**, *1*, 168.
[64] S. M. Emam, S. A. AbouEl-Enein, S. M. El-Seady, *J. Chin. Chem. Soc.* **2017**, *64*, 261.
[65] a) N. Kavitha, P. V. A. Lakshmi, *J. Saudi Chem. Soc.* **2017**, *21*, S457; b) A. P. Mishra, R. K. Jain, *J. Saudi Chem. Soc.* **2014**, *18*, 814.
[66] A. B. P. Lever, *Inorganic Electronic Spectroscopy*, Elsevier, Amsterdam **1968**.
[67] S. M. Emam, T. El Sayed, N. Nassar, *Spectrochim. Acta A* **2015**, *138*, 942.
[68] A. F. Shoair, A. A. El-Bindary, N. A. El-Ghamaz, G. N. Rezk, *J. Mol. Liq.* **2018**, *269*, 619.
[69] H. A. El-Boraey, *J. Therm. Anal. Calorim.* **2005**, *81*, 339.
[70] S. M. Emam, *J. Mol. Struct.* **2017**, *1134*, 444.
[71] E.-S. A. El-Samanody, S. A. AbouEl-Enein, E. M. Emara, *Appl. Organomet. Chem.* **2018**, *33*, 1.
[72] A. M. Donia, *Thermochim. Acta* **1998**, *320*, 187.
[73] H. A. El-Boraey, F. A. El-Saied, S. A. Aly, *J. Therm. Anal. Calorim.* **2009**, *96*, 599.
[74] F. A. El-Saied, S. A. AbouEl-Enein, S. M. Emam, H. A. El-Shater, *Polish J. Chem.* **2009**, *83*, 1871.
[75] T. Rosu, M. Negoiu, S. Pasculescu, E. Pahontu, D. Poirier, A. Gulea, *Eur. J. Med. Chem.* **2010**, *45*, 774.
[76] B. J. Hathaway, D. E. Billing, *Coord. Chem. Rev.* **1970**, *6*, 143.
[77] R. G. Pearson, *J. Chem. Sci.* **2005**, *117*, 369.
[78] S. Kaya, C. Kaya, *Mol. Phys.* **2015**, *113*, 1311.
[79] B. J. Hathaway, G. Wilkinson, R. Gillard, J. McCleverty, *Comprehensive Coordination Chemistry*, Vol. 5, Pergamon, Oxford **1987**.
[80] C. K. Kim, K. A. Lee, C. K. Kim, B.-S. Lee, H. W. Lee, *Chem. Phys. Lett.* **2004**, *391*, 321.
[81] R. Parthasarathi, V. Subramanian, D. R. Royb, P. K. Chattarajb, *Bioorg. Med. Chem.* **2004**, *12*, 5533.
[82] B. G. Tweedy, *Phytopathology* **1964**, *55*, 910.
[83] S. I. Al-Resayes, M. Shakir, N. Shahid, M. Azam, A. U. Khan, *Arab. J. Chem.* **2016**, *9*, 335.

SUPPORTING INFORMATION

Additional supporting information may be found online in the Supporting Information section at the end of this article.

How to cite this article: Emam SM, Tolan DA, El-Nahas AM. Synthesis, structural, spectroscopic, and thermal studies of some transition-metal complexes of a ligand containing the amino mercapto triazole moiety. *Appl Organometal Chem*. 2020;e5591. https://doi.org/10.1002/aoc.5591